Mechanisms Governing Target Search and Binding Dynamics of Hypoxia-Inducible Factors

Yu Chen[1,2,3], Claudia Cattoglio[1,2,3], Gina Dailey[1,3], Qiulin Zhu[1,3], Robert Tjian[1,2,3] *, and Xavier Darzacq[1,3] *

[1] Department of Molecular and Cell Biology, University of California, Berkeley, CA, USA.
[2] Howard Hughes Medical Institute, University of California, Berkeley, CA, USA.
[3] Li Ka Shing Center for Biomedical & Health Sciences, University of California, Berkeley, CA, USA.

*Correspondence: R.T. (jmlim@berkeley.edu), X.D. (darzacq@berkeley.edu)

Abstract

Transcription factors (TFs) are classically attributed a modular construction, containing well-structured sequence specific DNA-binding domains (DBDs) paired with disordered activation domains (ADs) responsible for protein-protein interactions targeting cofactors or the core transcription initiation machinery. However, this simple division of labor model struggles to explain why TFs with identical DNA binding sequence specificity determined *in vitro* exhibit distinct non-overlapping binding profiles *in vivo*. The family of Hypoxia-Inducible Factors (HIFs) offer a stark example: aberrantly expressed in several cancer types, HIF-1α and HIF-2α subunit isoforms recognize the same DNA motif *in vitro* – the hypoxia response element (HRE) – but only share a subset of their target genes *in vivo*, while eliciting contrasting effects on cancer development and progression under certain circumstances. To probe the mechanisms mediating isoform-specific gene regulation, we used live cell single particle tracking (SPT) to investigate HIF nuclear dynamics and how they change upon genetic perturbation or drug treatment. We found that HIF-α subunits and their dimerization partner HIF-1β exhibit distinct diffusion and binding characteristics that are exquisitely sensitive to concentration and subunit stoichiometry. Using domain-swap variants, mutations, and a HIF-2α specific inhibitor, we found that although the DBD and dimerization domains are important, a major determinant of chromatin binding and diffusion behavior is dictated by the AD-containing intrinsically disordered regions. These findings reveal a previously unappreciated role of IDRs in regulating the TF search process that may play a role in selective functional target site binding on chromatin.

Introduction

Sequence-specific transcription factors (TFs) are key frontline regulators of gene expression. Classical LexA-Gal4 domain-swap experiments in yeast presented a simple modular structure and apparent division of labor for typical TFs (Brent and Ptashne, 1985). In this textbook paradigm, the DNA-binding domain (DBD) is responsible for DNA sequence recognition and binding specificity while the activation domain (AD) is responsible for target gene transactivation that involves protein-protein interactions with co-factors, the basal transcription machinery and other ancillary factors that are generally devoid of sequence specific DNA recognition. In higher eukaryotes, each DBD class usually contains multiple closely related family members. For example, the bHLH class of TFs includes MyoD, Clock, and Max. They all recognize the same E-box DNA binding sequence motif 5'-CACGTG-3', yet each differentially regulates muscle differentiation, circadian rhythm, and cell proliferation, respectively (Kribelbauer et al., 2019). This raises the specificity paradox: how do TFs with seemingly identical DNA sequence specificity, at least as determined *in vitro*, nevertheless exhibit non-overlapping binding profiles *in vivo* and carry out distinct and even opposing functions? In general, when confronted with this conundrum, we have assumed that one or more co-factors or perhaps still to be identified "silent partner" TFs can somehow divert target recognition to a composite cis-regulatory site distinct from the canonical DNA binding site. Given the high occurrence of short binding motifs for most TFs throughout the genome, even with co-operative binding to composite sites, most potential specific binding sites nevertheless remain unoccupied as determined by genome-wide TF binding studies. What feature or motif within TFs outside of the DBD and dimerization domain may be responsible for such differential site selection has remained unclear. Thus, the simple rule of modular units with well separated divisions of labor between DBD, dimerization and transactivation may deserve a closer look. We also wondered whether quantitative single molecule dynamics measurements might reveal new aspects of TF behavior in living cells that could inform us regarding potential mechanisms influencing the target search process and differential site selectivity in a native physiologically relevant context.

Here we have chosen the Hypoxia-Inducible Factors (HIFs) as a representative example to study the paradox of highly conserved DBDs carrying out distinct target site selection and to dissect potential novel features of TFs that mediate chromatin binding. HIFs are a family of α/β heterodimeric TFs stabilized under hypoxic conditions to promote angiogenesis, anaerobic metabolism, cell proliferation and "stemness" (Semenza, 2012). The oxygen-labile alpha subunits (mainly HIF-1α and HIF-2α) complex with their oxygen-stable beta partner (mainly HIF-1β) to form

68 a functional dimer (Fig. 1A). All HIF subunit isoforms belong to the bHLH-PAS (Basic helix-loop-
69 helix-PER-ARNT-SIM) family, where the N-termini are structured domains containing bHLH (DNA
70 binding) and PAS (dimerization) domains, while the C-termini consist of intrinsically disordered
71 regions (IDRs) containing ADs (Fig. 1A and Fig. S1). HIF-1α/1β and HIF-2α/1β dimers share a
72 conserved structural fold (Wu et al., 2015), recognize the same hypoxia response element (HRE)
73 5'-TACGTG-3' binding motif (Schödel et al., 2011; Wenger et al., 2005), but share only a partial
74 overlap of target genes *in vivo* (Smythies et al., 2019). With their own unique target gene sets,
75 HIF-1α and -2α can exert divergent and even contrasting functions (Keith et al., 2012). For
76 example, while both HIF-1α and HIF-2α regulate angiogenesis, HIF-1α specifically regulates
77 glycolysis, apoptosis, and promotes NO production, whereas HIF-2α binds to the *POU5F1* locus
78 to maintain Oct4-regulated stem cell identity and pluripotency, promotes cell cycle progression,
79 and inhibits NO production (Keith et al., 2012; Smythies et al., 2019). Therefore, our current simple
80 textbook model of exchangeable modular TF functional units does not satisfactorily explain such
81 isoform-specific target gene regulation.
82
83 The HIF family differential specificity paradox is even more daunting to comprehend at the level
84 of disease inducing mechanisms. HIFs are aberrantly upregulated and recognized as oncogenic
85 drivers in multiple cancers. However, in addition to their shared roles in cancer onset and
86 progression, HIF-1α and -2α also show many independent, sometimes even opposing roles in
87 specific contexts (Keith et al., 2012). For example, in clear cell renal cell carcinoma (ccRCC), HIF-
88 2α is the critical tumorigenic driver whereas HIF-1α, in contrast with its usual tumorigenic role, is
89 mostly tumor-suppressive (Raval et al., 2005; Schödel et al., 2016). The regulatory mechanism
90 behind such highly divergent outcomes is still largely unknown. Given such complexity, without a
91 deeper understanding of isoform-specific transcriptional regulation, it is hard to predict the
92 functional outcomes mediated by individual HIF isoform in various cancer types or stages, which
93 could be a complicating factor in developing more effective HIF-targeting cancer therapeutics.
94
95 In this study, we aim to understand the molecular mechanisms mediating isoform-specific target
96 gene regulation at its most fundamental level – could we detect differential molecular dynamics
97 of distinct TF isoforms during the target search and chromatin binding process in live cells? Which
98 regions or domains of TFs might be responsible for such isoform specific properties? Could we
99 begin to discern possible mechanisms that guide TFs with highly conserved DBDs to their distinct
100 and specific targets beyond cognate DNA sequence recognition? Here we use HIFs as an
101 illustrative example, combining endogenous tagging and super-resolution single particle tracking

102 (SPT) (Liu et al., 2015) to study the dynamic behavior of these key gene regulators in live cells
103 under physiological conditions. We also dissect the contribution of different domains of HIF-α
104 isoforms by a series of mutation and domain swap experiments to directly test the concept of
105 modular functional domains. Deploying a combination of genetic and small-molecule
106 perturbations, we found that, although HIF DBD and dimerization are important for DNA target
107 acquisition, the amount of protein bound and its diffusion characteristics are mainly driven by
108 regions outside the DBD and dimerization domains. Our results reveal a previously unappreciated
109 role of unstructured domains in the target search and binding properties of TFs to functional
110 chromatin sites in live cancer cell context.
111
112 **Results**
113
114 **Establishing a human cancer cell system for live-cell single molecule imaging of HIF**
115 To investigate HIF dynamics, we first focused on one of the cognate dimers: HIF-2α/1β. We used
116 the common ccRCC line 786-O (Brodaczewska et al., 2016), derived from a VHL-deficient, H2
117 type primary clear cell renal cell carcinoma, wherein HIF-2α is stabilized due to an inactivating
118 mutation in VHL (the E3 ubiquitin ligase that targets all HIF-α isoforms for proteasomal
119 degradation)(Gnarra et al., 1994). The 786-O line also conveniently lacks any functional HIF-1α
120 due to a truncating mutation of HIF-1α (Shen et al., 2011; Swiatek et al., 2020), which allows us
121 to study one α isoform independently from the other. Using CRISPR/Cas9-mediated genome
122 editing, we successfully generated several clonal lines with homozygous knock-in (KIN) of the
123 HaloTag (Los et al., 2008) at the N-terminus of either HIF-2α or its binding partner, HIF-1β (Fig.
124 1B and Fig. S2, A-C). Western blotting confirmed that the tagged proteins are expressed at levels
125 similar to wild-type (WT) in unedited cells (e.g., HIF-2α clone A31 and HIF-1β clone A21) (Fig.
126 1B). Confocal imaging after covalently labeling cells with a fluorescent Halo-binding ligand
127 (JFX646) (Grimm et al., 2021) shows the expected nuclear localization for both Halo-HIF-2α and
128 Halo-HIF-1β proteins (Fig. 1C). In addition, using ChIP-seq, we confirmed that both tagged
129 proteins maintain a similar genome-wide binding profile as the WT protein in unedited cells (Fig.
130 S2D). We have thus established a human cancer cell system suitable for live-cell imaging on HIF-
131 2α and HIF-1β at endogenous expression levels.
132
133 To evaluate how HIF-2α and -1β explore the nucleus and bind DNA, we used the fast modality of
134 super resolution live cell single particle tracking (fSPT) that is capable of tracking rapidly diffusing
135 molecules. Cells with either HIF-2α or HIF-1β Halo KIN were doubly labeled with the live-cell

136 permeable Halo-binding JFX dyes (Fig. 1D) and were imaged under highly inclined and laminated
137 optical sheet illumination (HiLo) (Tokunaga et al., 2008) at high frame rates to capture the
138 movement of single molecules in their native nuclear environment (Fig. 1E). Stroboscopic
139 illumination at high excitation power is used to minimize motion blur, while sparse labeling ensures
140 only a limited number of molecules are detected at any given time in the nucleus to minimize
141 misconnections when computing the path of individual molecules (trajectories) (Fig. 1E and F).
142 We can then estimate relevant kinetic parameters from these trajectories, extracting quantitative
143 information such as diffusion coefficients and bound fraction.
144
145 **fSPT detects various HIF molecular states in their native nuclear environment**
146 To quantitatively analyze the acquired fSPT data, we used a non-parametric Bayesian approach
147 (Heckert et al., 2021) recently developed in our lab. We chose to use this new method, because
148 as dimeric transcription factors, HIF subunits could conceivably exist in multiple states (e.g.,
149 bound, moving as a monomer, moving as a dimer, and moving in a bigger complex containing
150 co-regulators) (Fig. 2A and 2B). One feature distinct from our previous approach, which required
151 the assumption of a fixed and limited (3 or less) number of states for the tracked protein (Hansen
152 et al., 2018), our new data analysis method does not require *a priori* knowledge of how many
153 underlying states exist for each tracked protein. Instead, it estimates the constituents in a range
154 of dynamic states with diffusion rates from 0.01 to 100 $\mu m^2 s^{-1}$ while accounting for known
155 experimental biases due to localization error and fluorophore defocalization (Heckert et al., 2021).
156 After aggregating all trajectories from all the cells examined, we generate a distribution of diffusion
157 coefficient estimates that reports the fraction of stably bound molecules while simultaneously
158 displaying the full behavioral spectrum of the diffusing molecules (Heckert et al., 2021) (Fig. 2C).
159
160 We observed highly heterogeneous results for both HIF-2α and HIF-1β, with varied diffusion
161 coefficient estimates from cell to cell, when applying the likelihood estimation to individual cells
162 (Fig. 2A and 2B, Fig. S3A, clones A31 and A21). These results indicate that for both HIF proteins,
163 a range of moving states likely exists. We then pooled trajectories from many cells (n ~60) to
164 estimate the distribution of diffusion coefficients for the population. Strikingly, we observed a very
165 different behavior for Halo-HIF-2α compared to Halo-HIF-1β. Whereas a large fraction (about 40%)
166 of Halo-HIF-2α is immobile and presumably chromatin-bound (defined as the fraction with a
167 diffusion coefficient < 0.1 μm^2/sec), the majority (above 70%) of Halo-HIF-1β appears freely
168 diffusing (Fig. 2C and S3B, clones A31 and A21). Also, the overall diffusion coefficient for the
169 Halo-HIF-1β mobile population is much larger than that of Halo-HIF-2α. We repeated

170 measurements in different KIN clones and confirmed the reproducibility of these results for both
171 Halo-HIF-2α (Fig. S3A-B, clone B50) and Halo-HIF-1β (Fig. S3A-B, clone B89). The differences
172 between HIF-2α and -1β seem counterintuitive at first, because one would expect HIF-2α and
173 HIF-1β to behave similarly since they should exist as a hetero-dimer. However, since the
174 endogenous HIF-1β is expressed at a much higher level than HIF-2α (Fig. S2C), the majority of
175 HIF-1β is free to diffuse without HIF-2α. Of note, the distribution plot only reflects the fraction of
176 molecules as a function of their diffusion coefficient, but does not report on the absolute number
177 of molecules. Therefore, a smaller bound fraction for Halo-HIF-1β does not mean fewer numbers
178 of bound molecules than Halo-HIF-2α, since many more Halo-HIF-1β molecules are present in
179 the nucleus. Given this scenario, we hypothesized that HIF-1β molecular dynamics and percent
180 binding should be modulated by changing the 2α/1β stoichiometry.
181
182 **HIF-1β binding and diffusing dynamics can be modulated by HIF-α:β stoichiometry, and**
183 **are dependent on dimerization**
184 To test the hypothesis that HIF-1β dynamics depends on 2α/1β ratio, we first tried to modulate its
185 behavior by stably over-expressing HIF-2α in the endogenously HIF-1β Halo-tagged KIN line (Fig.
186 2D). We found that the mobile population of Halo-HIF-1β diffuses more slowly when HIF-2α is
187 overexpressed, most likely due to its dimerization with the extra HIF-2α to form dimers capable of
188 DNA/chromatin binding. As expected, we also observed a significant increase in the Halo-HIF-1β
189 bound fraction (up to 50%), (Fig. 2E, Fig. S3C top and middle). To confirm that the changes in
190 HIF-1β dynamics caused by increasing levels of HIF-2α are dependent on hetero-dimerization,
191 we stably overexpressed the HIF-2α R171A/V192D double mutant (HIF-2α DM) that was
192 previously reported to lose its dimerization capability with HIF-1β (Wu et al., 2015). As expected,
193 overexpression of HIF-2α DM did not increase the bound fraction or decrease the overall diffusion
194 speed of Halo-HIF-1β to the same extent seen with WT HIF-2α overexpression (Fig. 2E, Fig. S3C
195 bottom), suggesting that the changes we observe are dimerization-dependent.
196
197 We further validated our results by stably overexpressing different forms of HIF-α in the HIF-1β
198 Halo-tagged KIN line and treating cells with a HIF-2α-specific small molecule inhibitor, Belzutifan
199 (PT-2977). Belzutifan inhibits HIF-2α/1β, but not HIF-1α/1β, dimerization by specifically binding
200 to the dimerization domain of HIF-2α (Fig. S4A), and thus has been used as an HIF-2α inhibitor
201 for ccRCC treatment (Wallace et al., 2016; Xu et al., 2019). We first confirmed that Belzutifan
202 inhibits HIF-2α transcription function in a dose-dependent manner (Fig. S4B). Importantly,
203 Belzutifan also reduces the HIF-2α bound fraction in the HIF-2α Halo-tagged KIN line in a similar

204 dosage-dependent manner, again revealing the potential of fSPT to measure TF dynamics and
205 associated functional changes (Fig. S4, C-E). We choose to use 0.2 μM Belzutifan for all
206 subsequent experiments to maximize its effect.
207
208 Next, we carried out a series of experiments designed to probe the consequences of swapping
209 different functional domains of HIF-1α and HIF-2α to determine which parts of these closely
210 related TFs might be involved in selective activities when paired with HIF-1β. Using the HIF-1β
211 Halo-tagged KIN line as the parental line, we stably overexpressed WT or chimeric HIF-α, where
212 we swapped the structured and disordered domains between HIF-1α and HIF-2α (Fig. 3A). All
213 these different HIF-α variants are expressed from a relatively strong EF-1alpha promoter and are
214 N-terminally 3xFLAG-tagged. A construct that expresses 3xFLAG only is used as control. We
215 then treated these cells with either Belzutifan or DMSO control and measured Halo-HIF-1β
216 dynamics (Fig. 3A). While 3xFLAG tag had no effect, overexpressing HIF-α, regardless of which
217 variant form, is able to both increase the bound fraction and reduce the overall diffusion speed of
218 HIF-1β (Fig. 3B top, and 3C, DMSO group). For cells overexpressing the α variants that contain
219 the HIF-2α structured domain, this effect on HIF-1β can be at least partially reverted after
220 Belzutifan treatment (Fig. 3B and 3C, +HIF-2α and +HIF-2α/1α). In contrast, for cells
221 overexpressing the α variants that contain the HIF-1α structured domain, this effect is resistant to
222 Belzutifan, consistent with the subunit isoform specificity of the drug for HIF-2α (Fig. 3B and 3C,
223 +HIF-1α and +HIF-1α/2α). In untransfected and 3xFLAG only overexpressing control cells,
224 treatment with Belzutifan only weakly reduces the HIF-1β bound fraction, again suggesting that
225 the majority of HIF-1β is not engaged with 2α (Fig. 3B and 3C, parental cell and +3xF). Overall,
226 these results demonstrate that HIF-1β dynamics change after engagement with its α partner and
227 can be selectively inhibited with a specific dimerization inhibitor. The observed differences also
228 confirm that fSPT is a powerful platform to monitor molecular dynamic changes of TFs in living
229 cells thus, allowing us to gain new mechanistic insights while we introduce various perturbations,
230 such as subunit concentration or stoichiometry and specific mutations.
231
232 **Regions outside the DBD/dimerization domain determine HIF molecular dynamics**
233 Interestingly, comparing the effects of the four different α variants, we found that regardless of
234 their structured domain, those with the same C terminal IDRs behave similarly (Fig 3B and 3C,
235 middle and right). Specifically, the variants containing the HIF-2α IDR have a stronger effect on
236 increasing HIF-1β binding than the variants containing the HIF-1α IDR. Thus, surprisingly, it
237 appears that the bound fraction of HIF-1β is not determined by the HIF-α DBD, but rather by HIF-

238 α IDR, which we found rather counterintuitive. To confirm the importance of HIF-α IDRs in HIF
239 binding, we overexpressed a truncated version of either HIF-1α or 2α that contains only the N-
240 terminal structured region (HIF-1α NT or HIF-2α NT), which still maintains both the DBD and
241 dimerization capability for interacting with HIF-1β (Wu et al., 2015). Indeed, both these truncated
242 forms lacking the IDR/AD of HIF-α minimally affect the HIF-1β bound fraction (Fig. S5).
243 Surprisingly, these truncated HIF-α variants also only marginally influenced the overall HIF-1β
244 diffusion speed. These results indicate that dimerization alone neither increases HIF-1β binding
245 nor reduces the overall diffusion speed of its moving population. Instead, the extended HIF-α AD-
246 containing IDR is necessary to influence and direct HIF-1β behavior.
247
248 To further test our hypothesis that HIF chromatin binding and the dynamics of the diffusion
249 population are dominated by the α subunit IDR, we switched to image the α subunit itself. We
250 made different forms of Halo-tagged HIF-α (WT and domain-swapped), stably but weakly
251 expressed them in WT 786-O cells with an L30 promoter (Fig. 4A). We first confirmed that binding
252 and diffusion characteristics of L30-expressed Halo-HIF-2α are very similar to the endogenous
253 Halo-HIF-2α in the KIN line (Fig. S6), demonstrating that weak overexpression can largely
254 recapitulate endogenous protein behavior. Therefore, this system provides a convenient tool to
255 investigate the contribution of each domain of HIF-α in the target search and binding process.
256 Much like our results with endogenous HIF-1β, we observed similar behaviors of HIF-α proteins
257 if they contain the same IDR (Fig. 4B top and middle), while displaying distinct behaviors when
258 endowed with different IDR isoforms (Fig. 4B bottom). Regardless of which DBD they have, the
259 variants containing the HIF-2α IDR (WT HIF-2α and HIF-1α/2α) show a higher bound fraction,
260 compared to the ones containing HIF-1α IDR (WT HIF-1α and HIF-2α/1α) (Fig. 4C). These results
261 suggest that indeed the disordered region on HIF-α determines how HIFs bind and diffuse in the
262 nucleus, and that the HIF-2α AD-containing IDR mediates HIF binding to chromatin and/or some
263 other relatively immobile components in 786-O cells.
264
265 **HIF-α disordered region is necessary but not sufficient for optimal binding**
266 The fact that the extent of binding (presumably to chromatin) of HIF proteins depends mainly on
267 the long C-terminal IDR rather than on their DBD was unexpected. Therefore, we next examined
268 the contribution of the HIF DBD to the bound fraction. We introduced point mutations in the DBD
269 (HIF-2α R27E and HIF-1α R30E) that were previously reported to impair DNA binding (Michel et
270 al., 2002; Wu et al., 2015), and expressed them in the WT 786-O cells with the same L30 promoter
271 system (Fig. 5A). Not surprisingly, DBD mutants show a reduction in the bound fraction and a

272 concomitant increase in the diffusing fraction compared to their WT counterpart (Fig. 5B and 5C).
273 In agreement with the expectation that the DBD mutations should not perturb protein-protein
274 interactions, we do not observe a significant change in the overall speed of the diffusing population.
275 These results demonstrate that, although the AD-containing IDR is the major modulator in
276 determining the bound fraction, the DBD is also important for binding, further suggesting that the
277 observed bound fraction likely represents chromatin/DNA binding.
278
279 We next examined whether dimerization with HIF-1β is required for HIF-α chromatin binding.
280 Taking advantage of the same L30 weak expression system, we exogenously expressed the
281 Halo-HIF-2α dimerization mutant (R171A/V192D), or the analogous Halo-HIF-1α dimerization
282 mutant (R170A/V191D) in the WT 786-O cells (Fig. 5D). We found that compared to the WT Halo-
283 HIF-2α or -1α, these mutants exhibit a significantly decreased bound fraction (Fig. 5E and 5F),
284 demonstrating that HIF-α without -1β can no longer effectively bind to DNA/chromatin. Taken
285 together, our results indicate that the HIF-α disordered region alone is not sufficient to maintain
286 binding, but instead, the IDR and both the DBD and dimerization domains are also needed.
287
288 **Intrinsic properties of HIF-α IDR determine the overall speed of diffusive HIF.**
289 Interestingly, with the Halo-HIF-α dimerization mutants, we observed no obvious change in their
290 overall diffusion coefficient in the moving population (Fig. 5E), indicating that losing their HIF-1β
291 partner does not affect the overall HIF-α diffusion speed. This result suggests that it is some
292 intrinsic property of HIF-α molecules, rather than the molecular weight of dimers versus
293 monomers, that determines its diffusion speed and behavior. Our results suggest that while the
294 moving population of HIF-1β alone diffuses relatively fast, the moving population of both HIF-α
295 and HIF- α/β dimers diffuses relatively slowly. We postulate this is potentially due to the HIF-α
296 IDR engaging in protein-protein interactions with various cofactors both when associated with
297 HIF-1β or when alone. (Fig. 6A). Indeed, this is consistent with our previous observation that the
298 HIF-a NT/HIF-1β dimer diffuses at a relatively fast speed, similar to HIF-1β alone which apparently
299 does not share this HIF-α IDR mediated capacity (Fig. S5).
300
301 **Discussion**
302 Transcription factors must search, recognize and bind to their specific target sites among millions
303 of possible DNA sequences along chromatin to activate the correct gene. With the successful
304 development of X-ray crystallography and cryo-EM, mechanisms of DNA-binding specificity have
305 been extensively studied, primarily based on classically structured globular DNA-binding domains

306 of TFs. We now know that a variety of structural mechanisms are used to recognize DNA,
307 including formation of specific hydrogen bonds and DNA contour interactions (Rohs et al., 2010).
308 However, these inherent binding modalities of DBDs alone cannot explain TF binding site
309 selection *in vivo*. As revealed by genome-wide *in vivo* binding assays, only a subset of potential
310 target sites become occupied, and this is not entirely consistent with either DNA binding site
311 affinity or chromatin accessibility (Behera et al., 2018; Grossman et al., 2017; Srivastava and
312 Mahony, 2020). On the other hand, TFs have long been recognized to also contain long
313 unstructured transactivation domains with simple amino acid composition (Gln-rich, acidic, Pro-
314 rich etc.), which often posed challenges to purification and/or crystallization of full-length TFs
315 (Courey and Tjian, 1988; Ma and Ptashne, 1987; Mermod et al., 1989; Tjian and Maniatis, 1994).
316 Recently, such intrinsically disordered regions (IDRs) were reported to play an important role in
317 weak and multivalent protein-protein interactions to form local small transient hubs that, when
318 exacerbated by overexpression, can drive phase separation. Although not structurally defined,
319 these interactions can still be sequence/amino acid composition selective (Chong et al., 2018;
320 Chong and Mir, 2021). IDRs are now proposed to have important functions in boosting gene
321 expression through hub or condensate formation to locally enrich for factors that are needed for
322 transcription (Boijja et al., 2018; Cho et al., 2018; Chong et al., 2018; Sabari et al., 2018; Wei et
323 al., 2020). However, few studies of IDRs have investigated their potential role in DNA binding site
324 search and selection. Some studies reported that for a subset of zinc finger proteins (Sp2 and
325 KLF3), an IDR is critical for *in vivo* binding and specificity (Burdach et al., 2014; Lim et al., 2016;
326 Völkel et al., 2015), and another recent study using genomic approaches reports the IDR as a
327 determinant for specificity of the yeast bZIP TF Yap1 (Brodsky et al., 2020).
328
329 Here, using advanced live cell single particle tracking, we report that TF IDRs previously
330 associated with ADs are, in fact, a major determinant mediating nuclear search dynamics and
331 chromatin binding characteristics. Employing both genetic and small molecule perturbations
332 together with a series of domain-swap and mutation experiments, we found that it is the AD
333 associated disordered region of HIF-α rather than the intrinsic molecular weight of the TF that
334 dictates a relatively slow diffusion for both HIF-α monomers and HIF-α/β dimers. On the other
335 hand, when not engaged with HIF-α, HIF-1β diffuses rapidly as expected for an unencumbered
336 subunit. These results indicate that the diffusion characteristic of HIF molecules is profoundly
337 influenced by the properties of their disordered regions (Fig. 6A). In fact, computational analysis
338 shows very different amino acid composition bias among HIF-1α, -2α and -1β disordered regions
339 (Fig. S1B). Thus, it is very likely that as these molecules navigate through the crowded nuclear

environment, their distinct stretches of IDRs that also contain ADs make differential and selective interactions with other nuclear components, resulting in distinct diffusive behaviors. It is also possible that due to differences in acidity, the different charges on these IDRs can cause differential interactions with macromolecules including not only proteins, but also DNA and RNA (Xiang et al., 2020).

While it is easy to conceptualize how IDRs can influence the speed of diffusion, one unexpected result is that they also largely determine how much and with what differential specificity TFs bind to chromatin. Although we confirmed that the DBD and dimerization domains are important for binding, the surprise was that our domain swap experiments clearly demonstrated that the percentage of bound TF is mainly contributed by regions outside of the DBD/dimerization domains. One explanation could be the differential charge propensities of the different disordered regions (Fig. S1B). For example, the HIF-2α IDR is more positively charged and may not only slow down nuclear exploration but also stabilize chromatin binding, possibly through stronger interactions with negatively charged chromatin-associated RNA and/or nucleosome-free DNA regions. Besides direct chromatin interactions, HIF-2α IDR could also increase and stabilize binding via indirect interactions with other chromatin-bound proteins. Moreover, since different IDRs can selectively interact with other IDRs (Chong et al., 2018; Chong and Mir, 2021), we also postulate that selective interactions with other TFs or co-regulators may play a role in determining HIF genome-binding specificity. One hint of such a “combinatorial TF selectivity mechanism” is that HIF-2α binding sites were frequently found adjacent to AP1/Fox binding sites, while HIF-1α binding sites were usually found next to HEY/SP1 binding sites (Smythies et al., 2019). It was also previously reported that while no target specificity was preserved in reporter gene assays, the N-terminal TAD of HIF-α conferred endogenous target specificity for two of the HIF-1 unique genes examined, possibly via specific interactions with transcriptional cofactors (Hu et al., 2007). Further Co-IP or pull-down assay coupled with mass spectrometry (MS) will be needed to more fully dissect this type of *in vivo* selectivity mechanism.

Finally, we have shown that our fSPT platform provides a powerful tool able to resolve *in vivo* protein dynamics that is exquisitely sensitive to concentration, subunit stoichiometry and genetic/small molecule perturbations. This is especially important when studying TFs, where a slight difference in expression level often generates completely different results, rendering over-expression systems highly susceptible to artifacts. It is also worth underscoring the importance of studying TFs in their native physiologically relevant chromatin environment, given their obligate

374 interactions with higher-order chromatin structures and cofactors. For example, the EPO gene is
375 reported to be responsive to HIF-2α but not HIF-1α in Hep3B cells (Warnecke et al., 2004) and in
376 murine liver (Rankin et al., 2007), however, a luciferase reporter driven by the upstream EPO
377 enhancer also responds strongly to HIF-1α (Varma and Cohen, 1997), which may generate
378 misleading results and interpretations. Our fSPT platform allows us to study transcriptional
379 regulation in the native chromatin context and with endogenous TF levels to obtain data with
380 physiological and functional relevance. Such live cell real time measurements under native cell
381 contexts could prove to be highly valuable, both for dissecting *in vivo* mechanisms of transcription
382 regulation, and for guiding the development of effective therapeutics. Our Belzutifan treatment
383 experiment is an example of how fSPT can reveal the mechanism of action of small molecule
384 inhibitors, and how it could serve as a powerful tool to screen for drugs that selectively target one
385 isoform versus another, using dimerization and binding readouts as indicators of efficacy and
386 specificity. Moreover, since our results demonstrated how IDRs can affect TF diffusion behavior,
387 potentially distinct dynamic features determined by a particular IDR can be exploited as a readout
388 for screening small molecules or peptides that target allosteric sites of TFs. Assays that can
389 quantitatively measure TF diffusive behavior in live cells could be transformative for advancing
390 drug discovery because a high throughput imaging strategy opens the door to effectively target
391 what has been traditionally considered "undruggable", such as most protein-protein interactions
392 including potentially unstructured TF activation domains.
393
394 In summary, using the HIF protein family as a case study, we uncovered a mechanism of IDR-
395 mediated nuclear search and differential chromatin binding. We expect this fundamental principle
396 to be applicable to a broad range of TF families.
397
398 **Materials and Methods**
399
400 **Cell culture, stable cell line construction and drug treatment**
401 Human 786-O clear cell renal carcinoma cells were obtained from the Cell Culture Facility at the
402 University of California at Berkeley, and were cultured at 37°C with 5% CO2 in 4.5 g/L glucose
403 DMEM (ThermoFisher, Waltham, MA, #10566016) supplemented with 10% Fetal Bovine Serum
404 (HyClone, Logan, UT, Cat. #SH30396.03, lot #AE28209315), 1 mM Sodium Pyruvate
405 (ThermoFisher #11360070) and 100 U/mL Penicillin-Streptomycin (ThermoFisher #15140122).
406 Cells were subcultured at a ratio of 1:4 to 1:12 every 2 to 4 days for no longer than 30 days.

407 Phenol red-free DMEM (ThermoFisher, #21063029) supplemented with 10% Fetal Bovine Serum,
408 1 mM Sodium Pyruvate and 100 U/mL Penicillin-Streptomycin was used for imaging.
409
410 Stable cell lines expressing the exogenous gene product (supplement table 1) were generated by
411 PiggyBac transposition and antibiotic selection. The gene of interest was cloned into a PiggyBac
412 vector which also co-expresses a puromycin resistant gene using Gibson Assembly and
413 confirmed by Sanger sequencing. Cells were transfected by nucleofection using the Lonza Cell
414 Line Nucleofector® Kit V (Lonza, Basel, Switzerland, #VVCA-1003) and the Amaxa Nucleofector
415 II device. For each transfection, cells were plated 1-2 days before nucleofection in a 15-cm dish,
416 and reached approximately 50-70% confluency on the day of nucleofection, which equals to
417 approximately 3-4 million cells. 2 µg of PiggyBac plasmid was co-transfected with 1 µg of
418 SuperPiggyBac transposase vector with the T-020 program according to manufacturer's protocol.
419 Transfected cells were cultured for 24-48 hours before changing to selection media. Cells were
420 then selected for 14 days with 1 µg/ml puromycin (ThermoFisher #A1113803) and stable cell lines
421 were maintained in selection media for up to 30 days of culturing.
422
423 For drug treatment, 100 mM Belzutifan stock solution was prepared by dissolving Belzutifan
424 power (CAS No: 1672668-24-4, MedChemExpress, Monmouth Junction, NJ, Cat. #HY-125840)
425 in DMSO (Sigma, St. Louis, MO, #D2650), and was diluted 1:500,000 in growth media to the final
426 concentration of 0.2 µM. The same volume of DMSO (0.0002%) is used in the reference group
427 as control. Cells were treated for 24 hours in either Belzutifan or DMSO alone before imaging.
428 For dosage-dependent assays in Figure S4, DMSO amount was kept the same (0.0002%) for all
429 drug concentrations.
430
431 **CRISPR/Cas9-mediated genome editing**
432 Knock-in cell lines were generated as previously described (Hansen et al., 2017) with the following
433 changes. For each editing case, we designed 3 sgRNAs using CRISPOR (Concordet and
434 Haeussler, 2018). For each guide/donor pair, approximately 4 million 786-O cells were
435 nucleofected with 3.75 µg of donor plasmid and 1.25 µg of sgRNA plasmid. 24 hours after
436 transfection, Venus-positive cells were sorted and cultured for another 5-7 days, then Halo-
437 positive cells were sorted individually into single wells of 96 well plates. Clones were expanded
438 and genotyped with two rounds of PCR. The first round used one primer upstream of the left
439 homologous arm and the other primer downstream of the right homologous arm. The second
440 round used either of the external primers and a corresponding internal primer located in the

441 HaloTag coding region. Homozygous clones with the correct genotype, including Halo-HIF-2α
442 KIN clone A31 and clone B50, Halo-HIF-1β KIN clone A21 and clone B89, were confirmed by
443 Sanger sequencing and western blotting.
444
445 **Cell preparation and dye labeling for imaging**
446 For fast SPT, cells were grown on sonicated and plasma-cleaned 25-mm circular no 1.5H
447 precision cover glass (Marienfeld, Germany, 0117650) in 6-well plate. At least one day before
448 imaging, selective medium (if used) was removed and replaced with non-selective growth medium.
449 On the day of imaging, cells should be less than 100% confluent. Immediately before imaging,
450 cells were double labeled with JFX dyes as follows: cells were first incubated for 5 min in 1 ml
451 growth medium containing JFX 646, at a concentration that only gives approximately 10 detected
452 molecules per frame in the initial frames to ensure minimum misconnection of trajectories
453 between detections. This concentration differs from cell line to cell line, ranging from 0.2 – 5 nM,
454 depending on the expression level of the Halo-fusion protein. After 5 min of incubation, medium
455 was removed, cells were rinsed in PBS, and incubated for 5 min in 1 ml medium containing JFX
456 549. The concentration of JFX 549 also varies, usually at 25x the concentration of JFX 646. After
457 incubation, cells were washed twice for 5 min each, a first time with 2 ml regular growth media,
458 and a second time with 2 ml phenol red-free growth media, with a quick PBS rinse before each
459 wash. After wash, coverslip was transferred to Attofluor Cell Chambers (ThermoFisher, #A7816)
460 with cells facing up and 1 ml phenol red-free medium added to the chamber. For Belzutifan
461 treatment experiments, Belzutifan or equivalent amount of DMSO was added throughout the
462 labeling and washing steps (except during PBS rinses), as well as in the final imaging medium,
463 at the indicated concentration.
464
465 **Live Cell Single particle tracking**
466 All SPT experiments were carried out on a custom-built microscope as previously described
467 (Hansen et al., 2017) (McSwiggen et al., 2019). In brief, a Nikon TI microscope is equipped with
468 a 100x/ NA 1.49 oil-immersion TIRF objective, a motorized mirror, a perfect Focus system, an
469 EM-CCD camera and an incubation chamber maintained with humidified atmosphere with 5%
470 CO2 at 37 °C. All microscope, camera and hardware components were controlled through the
471 NIS-Elements software (Nikon).
472
473 During imaging, samples were excited with 561-nm laser at 1100 mW (Genesis Coherent, Santa
474 Clara, CA) with emission filter set to Semrock 593/40 nm band-pass filter to locate and focus the

475 cell nuclei, as well as to adjust laser angle to achieve highly inclined laminated optical sheet (HiLo)
476 illumination (Tokunaga et al., 2008). An ROI (Regions of Interest) of random size was selected to
477 fit into the interior of the nuclei but with maximized area. Then the emission filter was switched to
478 Semrock 676/37 nm bandpass filter while keeping TIRF angle, stage xyz position and ROI the
479 same. Movies were then taken with 633-nm laser (Genesis Coherent, Santa Clara, CA) at 1100
480 mW and 1 ms pulse, with camera exposure at 5.48-ms frame rate for 800-1600 frames, until
481 samples were completely photo-bleached. At least 20 movies (corresponding to 20 cells) were
482 taken for each sample as one biological replicate on a given day. A total of three biological
483 replicates on three separate days were collected to produce the final results (>60 cells per cell
484 line/condition).
485
486 **SPT data processing**
487 Raw SPT movies were processed with a publicly available single particle tracking package
488 (https://github.com/alecheckert/quot) to generate trajectory files (.trajs). Generally, it performs
489 tracking in the following steps: read a frame, find spots in the frame, localize spots to subpixel
490 resolution, and reconnect spots from consecutive frames into trajectories. Since a non-
491 photoactivatable dye was used for all SPT experiments, we labeled cells with a dye concentration
492 that only gives very low spot detection density, which allowed us to track spots since the first
493 frame. This is important because if the initial frames are filtered due to high localization density,
494 there might be a bias towards moving molecules, due to the bound molecules being
495 photobleached and diffusing molecules moving into the focal plane during the later frames.
496 Although we used very sparse labeling, occasionally there would be frames with high density, to
497 minimize misconnections due to multiple particles in close proximity, we incorporated a filtering
498 step where we removed frames with more than 7 detections in the following way. First, we
499 computed the number of detections per frame. Next, this function was smoothed with uniform
500 filtering with a kernel width of 21 frames. Finally, we identified frames with fewer than 7 detections
501 after smoothing and isolated trajectories from these frames. Specifically, the following
502 configuration was used for all detections and tracking: Image reading and filtering settings: start
503 = 0, method = “identity”, chunk_size = 100; Spot detection settings: method = “llr”, k = 1.0, w = 15,
504 t = 18; Subpixel localization settings: method = 'ls_int_gaussian', window_size = 9, sigma = 1.0,
505 ridge = 0.001, max_iter = 20, damp = 0.3; Tracking settings: method = 'euclidean',
506 max_spots_per_frame = 7, pixel_size_um = 0.16, frame_interval = 0.00548, search_radius = 1.0,
507 max_blinks = 0, min_I0 = 0.0, scale = 7.0.
508

509 To infer the distribution of diffusion coefficients from experimentally observed trajectories, we
510 used a publicly available implementation of state arrays (https://github.com/alecheckert/spagl)
511 (`sample_script_fss.py`), which generates the posterior mean occupations for a state array
512 evaluated on trajectories across all cells. In all analyses, we used the likelihood function for
513 regular Brownian with localization error (RBME) (Heckert et al., 2021). Settings were:
514 frame_interval = 0.00548, pixel_size_um = 0.16, dz = 0.7. Occupations are reported as the
515 mean of the posterior distribution over state occupations, marginalized on diffusion coefficient.
516
517 To generate RBME likelihood for individual cells, we used the `sample_script_by_file.py`
518 script in the same repository (https://github.com/alecheckert/spagl) (Heckert et al., 2021) with
519 the following settings: frame_interval = 0.00548, dz = 0.7, pixel_size_um=0.16,
520 scale_by_total_track_count = True, scale_colors_by_group = True.
521
522 **Antibodies**
523 The following antibodies were used for ChIP-seq: rabbit polyclonal anti-HIF-2α (Novus Biologicals,
524 Centennial, CO, #NB100-122), mouse monoclonal anti-HIF-1β (Novus Biologicals, #NB100-124),
525 rabbit polyclonal anti-V5 (Abcam, Cambridge, UK, #ab9116). The following antibodies were used
526 for western blotting: rabbit monoclonal anti-HIF-2α (Cell Signaling, Danvers, MA, #D9E3) diluted
527 at 1:1000, rabbit monoclonal anti-HIF-1β (Cell Signaling, #D28F3) diluted at 1:1000, mouse
528 monoclonal anti-V5 tag (ThermoFisher, # R960-25) diluted at 1:2500, mouse monoclonal anti-
529 HaloTag (Promega, Madison, WI, # G9211) diluted at 1:1000, mouse monoclonal anti-TBP
530 (Abcam, #ab51841) diluted at 1:2500, goat-anti-mouse-HRP (ThermoFisher, #31430) diluted at
531 1:2000, goat-anti-rabbit-HRP (ThermoFisher, # 31462) diluted at 1:2000.
532
533 **Western blotting**
534 All western samples were prepared as follows: cells growing in either 6-well plates or 10-cm dish
535 in log phase were rinsed with PBS twice and lysed on ice in 100-500 ul 2x Sample buffer (80 mM
536 Tris pH6.8, 2% SDS, 10% Glycerol, 0.0006% Bromophenol blue) containing 280 mM 2-
537 Mercaptoethanol (Sigma #M7522), 1x Aprotinin (Sigma, #A6279, diluted 1:1000), 1 mM
538 Benzamidine (Sigma, #B6506), 1x cOmplete™ EDTA-free Protease Inhibitor Cocktail (Sigma,
539 #5056489001), and 0.25 mM PMSF (Sigma #11359061001). Cell lysates were scraped and
540 collected into 1.5-ml Eppendorf tubes, incubated at 99 °C with constant shaking, snap frozen in
541 liquid nitrogen and stored at -80 °C. On the day of western blotting, samples were thawed and
542 centrifuged at top speed for 5 min at 4 °C. Ten to 15 µl supernatant were loaded on an 8% SDS-

543 Page gel, ran for 1h at 200 V and 4 °C, and transferred to 0.45-µm nitrocellulose membrane
544 (Fisher, # 45004031) for 2 hrs at 100V. Membranes were blocked in 10% milk in 0.1% TBS-Tween
545 for 1 hr at RT, and incubated overnight at 4 °C with primary antibodies diluted in 5% milk in 0.1%
546 TBS-Tween. After 4 x 5 min washes in 0.1% TBS-Tween, membranes were incubated at RT for
547 at least 1 h with secondary antibodies diluted in 5% milk in 0.1% TBS-Tween. After 4 x 5 min
548 washes in 0.1% TBS-Tween, membranes were incubated for 3 min in freshly made Perkin Elmer
549 LLC Western Lightning Plus-ECL, Enhanced Chemiluminescence Substrate (Fisher,
550 #509049326), and imaged with a Bio-Rad ChemiDoc imaging system (BioRad, Model No:
551 Universal Hood III). For reblotting, membranes were immersed in Restore™ Western Blot
552 Stripping Buffer (Fisher, #21059) for 15 min at RT with shaking, washed 3 x 10 min in 0.1% TBS-
553 Tween, followed by blocking, antibody incubation and chemiluminescence reaction as described
554 above.
555
556 **Chromatin Immunoprecipitation and ChIP-seq library preparation**
557 ChIP was performed as described with few modifications (Testa et al., 2005). Wild type 786-O or
558 endogenously tagged knock-in clones A31 (V5-Halo-HIF-2α) and A21 (V5-Halo-HIF-1β) were
559 expanded to two 15-cm dishes and cross-linked 5' at room temperature with 1% formaldehyde-
560 containing FBS-free medium; cross-linking was stopped by adding PBS-glycine (0.125 M final).
561 Cells were washed twice with ice-cold PBS, scraped, centrifuged for 10' and pellets were flash-
562 frozen. Cell pellets were thawed and resuspended in 2 ml of cell lysis buffer (5 mM PIPES, pH
563 8.0, 85 mM KCl, and 0.5% NP-40, 1 ml/15 cm plate) w/ protease inhibitors and incubated for 10'
564 on ice. Lysates were centrifuged for 10' at 4000 rpm and nuclear pellets resuspended in 6 volumes
565 of sonication buffer (50 mM Tris-HCl, pH 8.1, 10 mM EDTA, 0.1% SDS) w/ protease inhibitors,
566 incubated on ice for 10', and sonicated to obtain DNA fragments around 500 bp in length (Covaris
567 S220 sonicator, 20% Duty factor, 200 cycles/burst, 150 peak incident power, 10 cycles 30" on
568 and 30" off). Sonicated lysates were cleared by centrifugation and chromatin (400 µg per antibody)
569 was diluted in RIPA buffer (10 mM Tris-HCl, pH 8.0, 1 mM EDTA, 0.5 mM EGTA, 1% Triton X-
570 100, 0.1% SDS, 0.1% Na-deoxycholate, 140 mM NaCl) w/ protease inhibitors to a final
571 concentration of 0.8 µg/µl, precleared with Protein G sepharose (GE Healthcare) for 2 hours at
572 4°C and immunoprecipitated overnight with 4 µg of specific antibodies. About 4% of the
573 precleared chromatin was saved as input. Immunoprecipitated DNA was purified with the Qiagen
574 QIAquick PCR Purification Kit, eluted in 33 µl of 0.1X TE (1 mM Tris-HCl pH 8.0, 0.01 mM EDTA)
575 and analyzed by qPCR together with 2% of the input chromatin prior to ChIP-seq library

576 preparation (SYBR® Select Master Mix for CFX, ThermoFisher). ChIP-qPCR primer sequences
577 were as follows:
578 hWISP1_positive_forward: TGAGGTCAGTGTGGTTTGGT
579 hWISP1_positive_reverse: ACATGGTCACGTAGCTAGCA
580 hWISP1_negative_forward: AGTCCCCAGCACATAGAAGG
581 hWISP1_negative_reverse: GGTTCTGAAGGTGACCGACT
582 ChIP-seq libraries were prepared using the NEBNext® Ultra™ II DNA Library Prep Kit for Illumina®
583 (NEB E7645) according to manufacturer instructions with a few modifications. 20 ng of ChIP input
584 DNA (as measured by Nanodrop) and 25 μl of the immunoprecipitated DNA were used as a
585 starting material and the recommended reagents' volumes were cut in half. The NEBNext Adaptor
586 for Illumina was diluted 1:10 in Tris/NaCl, pH 8.0 (10 mM Tris-HCl pH 8.0, 10 mM NaCl) and the
587 ligation step extended to 30'. After ligation, a single purification step with 0.9X volumes of
588 Agencourt AMPure XP PCR purification beads (Beckman Coulter A63880) was performed, eluting
589 DNA in 22 μl of 10 mM Tris-HCl pH 8.0. 20 μl of the eluted DNA were used for the library
590 enrichment step, performed with the KAPA HotStart PCR kit (Roche Diagnostics KK2502) in 50
591 μl of total reaction volume (10 μl 5X KAPA buffer, 1.5 μl 10 mM dNTPs, 0.5 μl 10 μM NEB
592 Universal PCR primer, 0.5 μl 10 μM NEB index primer, 1 μl KAPA polymerase, 16.5 μl nuclease-
593 free water and 20 μl sample). Samples were enriched with 9 PCR cycles (98 °C, 45"; [98 °C, 15";
594 60 °C, 10"] x 9; 72 °C, 1'; 4 °C, hold), purified with 0.9 volumes of AMPure XP PCR purification
595 beads and eluted with 33 μl of 10 mM Tris-HCl pH 8.0. Library concentration, quality and fragment
596 size were assessed by Qubit fluorometric quantification (Qubit™ dsDNA HS Assay Kit,
597 Invitrogen™ Q32851) qPCR and Fragment analyzer™. 12 multiplexed libraries (input, HIF1-β,
598 HIF1-α and V5 pulldowns in WT 786O cells and A31 and A21 clones) were pooled and sequenced
599 in one lane on the Illumina HiSeq4000 sequencing platform (50-bp, single end-reads) at the
600 Vincent J. Coates Genomics Sequencing Laboratory at UC Berkeley.
601
602 **ChIP-seq analysis**
603 ChIP-seq raw reads from WT 786O cells and A31 and A21 endogenously Halo-tagged clones (12
604 libraries total, 1 replicate per condition) were quality-checked with FastQC and aligned onto the
605 human genome (hg38 assembly) using Bowtie (Langmead et al., 2009), allowing for two
606 mismatches (-n 2) and no multiple alignments (-m 1). Peaks were called with MACS2 (--nomodel
607 --extsize 300) (Zhang et al., 2008) using input DNA as a control. To create heatmaps we used
608 deepTools (version 2.4.1) (Ramírez et al., 2016). We first ran bamCoverage (--binSize 50 --

609 normalizeTo1x 2913022398 --extendReads 300 --ignoreDuplicates -of bigwig) and normalized
610 read numbers to 1x sequencing depth, obtaining read coverage per 50-bp bins across the whole
611 genome (bigWig files). We then used the bigWig files to compute read numbers across 6 kb
612 centered on HIF-2α peaks called by MACS2 across all 786O cell lines, subtracted of V5 peaks
613 called by MACS2 in WT 786O cells (computeMatrix reference-point --referencePoint=TSS --
614 upstream 3000 --downstream 3000 --missingDataAsZero --sortRegions=no). We sorted the
615 output matrices by decreasing WT 786O enrichment, calculated as the total number of reads
616 within a MACS2 called ChIP-seq peak. Finally, heatmaps were created with the plotHeatmap tool
617 (--averageTypeSummaryPlot=mean --colorMap='Blues' --sortRegions=no).
618
619 **Luciferase reporter assay**
620 The firefly luciferase reporter gene construct was made by inserting a 3x Hypoxia Responsive
621 Elements (HREs) from the EPO gene enhancer (sequence:
622 tcgaagccctacgtgctgtctcacacagcctgtctgacctctcgacctaccggccgttcgaagccctacgtgctgtctcacacagccttct
623 gatctcgacctaccggccgttcgaagccctacgtgctgtctcacacagcctgtctgacctctcgacctaccggccgt) into the 5' of
624 the minimal TATA-box promoter in the pGL4.23 [luc2/minP] vector (Promega #E841A). A control
625 pHRL-TK vector (Promega #E2241) expressing *Renilla* luciferase with an HSV TK promoter was
626 used as reference to normalize luciferase activity. Cells were co-transfected with 1 ug of firefly
627 Luciferase vector and 0.1 ug *Renilla* luciferase vector by nucleofection with Lonza Cell Line
628 Nucleofector® Kit V (Lonza, #VVCA-1003) and the T-020 program in the Amaxa Nucleofector II
629 device. After nucleofection, cells were resuspended in complete growth medium, and plated into
630 12-well plates with Belzutifan added to various concentrations as indicated. 24 hours after
631 nucleofection, cells were lysed and luciferase activity was analyzed with Dual-luciferase Reporter
632 Assay System (Promega, #E1960) according to manufacturer's protocol. The relative luciferase
633 activity was calculated by normalizing firefly luciferase activity to the *Renilla* luciferase activity to
634 control for transfection efficiency.
635
636 **Datasets and accession numbers**
637 The ChIP-seq data generated in this publication have been deposited in NCBI's Gene Expression
638 Omnibus (Edgar et al., 2002) and are accessible through GEO Series accession number
639 GSE183900. SPT raw data are accessible through DOI: 10.5281/zenodo.5559234.
640
641 **Acknowledgments**

642 We thank Luke Lavis for providing fluorescent HaloTag ligands; the CRL Flow Cytometry Facility
643 for assistance with cell sorting; the QB3 High Throughput Screening Facility for providing access
644 to Opera Phenix automated confocal microscope; Dr. Alec Heckert for sharing data analysis
645 pipeline and usage instructions; Dr. Alec Heckert, Dr. Andrew Belmont, Dr. Max Staller, Dr.
646 Shasha Chong, Dr. Jiang Xu, and members of Tjian/Darzacq labs for helpful discussions and
647 critical reading of the manuscript. This work was supported by the NIH grant U54-CA231641-01
648 (to XD), and the Howard Hughes Medical Institute (to RT). This work used the Vincent J. Coates
649 Genomics Sequencing Laboratory at UC Berkeley, supported by NIH S10 OD018174
650 Instrumentation Grant.
651
652 **Author contributions:** YC designed experiments with guidance from XD and RT. YC, CC, GD
653 and QZ performed experiments. YC drafted the original manuscript. CC, XD and RT reviewed
654 and edited the manuscript. XD and RT supervised the project.
655
656 **Competing interests:** RT and XD are co-founders of Eikon Therapeutics.
657
658 **References**
659 Behera V, Evans P, Face CJ, Hamagami N, Sankaranarayanan L, Keller CA, Giardine B, Tan K,
660 Hardison RC, Shi J, Blobel GA. 2018. Exploiting genetic variation to uncover rules of
661 transcription factor binding and chromatin accessibility. *Nat Commun* **9**:782.
662 doi:10.1038/s41467-018-03082-6
663 Boijja A, Klein IA, Sabari BR, Dall'Agnese A, Coffey EL, Zamudio AV, Li CH, Shrinivas K,
664 Manteiga JC, Hannett NM, Abraham BJ, Afeyan LK, Guo YE, Rimel JK, Fant CB,
665 Schuijers J, Lee TI, Taatjes DJ, Young RA. 2018. Transcription factors activate genes
666 through the phase separation capacity of their activation domains. *Cell* **175**:1842.
667 doi:10.1016/j.cell.2018.10.042
668 Brent R, Ptashne M. 1985. A eukaryotic transcriptional activator bearing the DNA specificity of a
669 prokaryotic repressor. *Cell* **43**:729–736. doi:10.1016/0092-8674(85)90246-6
670 Brodaczewska KK, Szczylik C, Fiedorowicz M, Porta C, Czarnecka AM. 2016. Choosing the
671 right cell line for renal cell cancer research. *Mol Cancer* **15**:83. doi:10.1186/s12943-016-
672 0565-8
673 Brodsky S, Jana T, Mittelman K, Chapal M, Kumar DK, Carmi M, Barkai N. 2020. Intrinsically
674 Disordered Regions Direct Transcription Factor In Vivo Binding Specificity. *Mol Cell*
675 **79**:459-471.e4. doi:10.1016/j.molcel.2020.05.032

676 Burdach J, Funnell APW, Mak KS, Artuz CM, Wienert B, Lim WF, Tan LY, Pearson RCM,
677 Crossley M. 2014. Regions outside the DNA-binding domain are critical for proper in vivo
678 specificity of an archetypal zinc finger transcription factor. *Nucleic Acids Res* **42**:276–
679 289. doi:10.1093/nar/gkt895
680 Cho W-K, Spille J-H, Hecht M, Lee C, Li C, Grube V, Cisse II. 2018. Mediator and RNA
681 polymerase II clusters associate in transcription-dependent condensates. *Science*
682 **361**:412–415. doi:10.1126/science.aar4199
683 Chong S, Dugast-Darzacq C, Liu Z, Dong P, Dailey GM, Cattoglio C, Heckert A, Banala S, Lavis
684 L, Darzacq X, Tjian R. 2018. Imaging dynamic and selective low-complexity domain
685 interactions that control gene transcription. *Science* **361**:eaar2555.
686 doi:10.1126/science.aar2555
687 Chong S, Mir M. 2021. Towards Decoding the Sequence-Based Grammar Governing the
688 Functions of Intrinsically Disordered Protein Regions. *J Mol Biol* **433**:166724.
689 doi:10.1016/j.jmb.2020.11.023
690 Concordet J-P, Haeussler M. 2018. CRISPOR: intuitive guide selection for CRISPR/Cas9
691 genome editing experiments and screens. *Nucleic Acids Res* **46**:W242–W245.
692 doi:10.1093/nar/gky354
693 Courey AJ, Tjian R. 1988. Analysis of Sp1 in vivo reveals multiple transcriptional domains,
694 including a novel glutamine-rich activation motif. *Cell* **55**:887–898. doi:10.1016/0092-
695 8674(88)90144-4
696 Edgar R, Domrachev M, Lash AE. 2002. Gene Expression Omnibus: NCBI gene expression
697 and hybridization array data repository. *Nucleic Acids Res* **30**:207–210.
698 doi:10.1093/nar/30.1.207
699 Gaur RK. 2014. Amino acid frequency distribution among eukaryotic proteins. *IIOAB J* **5**:6–11.
700 Gnarra JR, Tory K, Weng Y, Schmidt L, Wei MH, Li H, Latif F, Liu S, Chen F, Duh FM. 1994.
701 Mutations of the VHL tumour suppressor gene in renal carcinoma. *Nat Genet* **7**:85–90.
702 doi:10.1038/ng0594-85
703 Grimm JB, Xie L, Casler JC, Patel R, Tkachuk AN, Falco N, Choi H, Lippincott-Schwartz J,
704 Brown TA, Glick BS, Liu Z, Lavis LD. 2021. A General Method to Improve Fluorophores
705 Using Deuterated Auxochromes. *Jacs Au* **1**:690–696. doi:10.1021/jacsau.1c00006
706 Grossman SR, Zhang X, Wang L, Engreitz J, Melnikov A, Rogov P, Tewhey R, Isakova A,
707 Deplancke B, Bernstein BE, Mikkelsen TS, Lander ES. 2017. Systematic dissection of
708 genomic features determining transcription factor binding and enhancer function. *Proc*
709 *Natl Acad Sci* **114**:E1291–E1300. doi:10.1073/pnas.1621150114

710 Hansen AS, Pustova I, Cattoglio C, Tjian R, Darzacq X. 2017. CTCF and cohesin regulate
711 chromatin loop stability with distinct dynamics. *eLife* **6**:e25776. doi:10.7554/eLife.25776
712 Hansen AS, Woringer M, Grimm JB, Lavis LD, Tjian R, Darzacq X. 2018. Robust model-based
713 analysis of single-particle tracking experiments with Spot-On. *eLife* **7**:e33125.
714 doi:10.7554/eLife.33125
715 Hanson J, Yang Y, Paliwal K, Zhou Y. 2017. Improving protein disorder prediction by deep
716 bidirectional long short-term memory recurrent neural networks. *Bioinformatics* **33**:685–
717 692. doi:10.1093/bioinformatics/btw678
718 Heckert A, Dahal L, Tjian R, Darzacq X. 2021. Recovering mixtures of fast diffusing states from
719 short single particle trajectories. bioRxiv. doi:10.1101/2021.05.03.442482
720 Hu C-J, Sataur A, Wang L, Chen H, Simon MC. 2007. The N-terminal transactivation domain
721 confers target gene specificity of hypoxia-inducible factors HIF-1alpha and HIF-2alpha.
722 *Mol Biol Cell* **18**:4528–4542. doi:10.1091/mbc.e06-05-0419
723 Keith B, Johnson RS, Simon MC. 2012. HIF1α and HIF2α: sibling rivalry in hypoxic tumour
724 growth and progression. *Nat Rev Cancer* **12**:9–22. doi:10.1038/nrc3183
725 Kribelbauer JF, Rastogi C, Bussemaker HJ, Mann RS. 2019. Low-Affinity Binding Sites and the
726 Transcription Factor Specificity Paradox in Eukaryotes. *Annu Rev Cell Dev Biol* **35**:357–
727 379. doi:10.1146/annurev-cellbio-100617-062719
728 Langmead B, Trapnell C, Pop M, Salzberg SL. 2009. Ultrafast and memory-efficient alignment
729 of short DNA sequences to the human genome. *Genome Biol* **10**:R25. doi:10.1186/gb-
730 2009-10-3-r25
731 Lim WF, Burdach J, Funnell APW, Pearson RCM, Quinlan KGR, Crossley M. 2016. Directing an
732 artificial zinc finger protein to new targets by fusion to a non-DNA-binding domain.
733 *Nucleic Acids Res* **44**:3118–3130. doi:10.1093/nar/gkv1380
734 Liu Z, Lavis LD, Betzig E. 2015. Imaging Live-Cell Dynamics and Structure at the Single-
735 Molecule Level. *Mol Cell* **58**:644–659. doi:10.1016/j.molcel.2015.02.033
736 Los GV, Encell LP, McDougall MG, Hartzell DD, Karassina N, Zimprich C, Wood MG, Learish R,
737 Ohana RF, Urh M, Simpson D, Mendez J, Zimmerman K, Otto P, Vidugiris G, Zhu J,
738 Darzins A, Klaubert DH, Bulleit RF, Wood KV. 2008. HaloTag: A Novel Protein Labeling
739 Technology for Cell Imaging and Protein Analysis. *ACS Chem Biol* **3**:373–382.
740 doi:10.1021/cb800025k
741 Ma J, Ptashne M. 1987. Deletion analysis of GAL4 defines two transcriptional activating
742 segments. *Cell* **48**:847–853. doi:10.1016/0092-8674(87)90081-X

743 McSwiggen DT, Hansen AS, Teves SS, Marie-Nelly H, Hao Y, Heckert AB, Umemoto KK,
744 Dugast-Darzacq C, Tjian R, Darzacq X. 2019. Evidence for DNA-mediated nuclear
745 compartmentalization distinct from phase separation. *eLife* **8**:e47098.
746 doi:10.7554/eLife.47098
747 Mermod N, O'Neill EA, Kelly TJ, Tjian R. 1989. The proline-rich transcriptional activator of
748 CTF/NF-I is distinct from the replication and DNA binding domain. *Cell* **58**:741–753.
749 doi:10.1016/0092-8674(89)90108-6
750 Michel G, Minet E, Mottet D, Remacle J, Michiels C. 2002. Site-directed mutagenesis studies of
751 the hypoxia-inducible factor-1α DNA-binding domain. *Biochim Biophys Acta BBA - Gene*
752 *Struct Expr* **1578**:73–83. doi:10.1016/S0167-4781(02)00484-0
753 Ramírez F, Ryan DP, Grüning B, Bhardwaj V, Kilpert F, Richter AS, Heyne S, Dündar F, Manke
754 T. 2016. deepTools2: a next generation web server for deep-sequencing data analysis.
755 *Nucleic Acids Res* **44**:W160-165. doi:10.1093/nar/gkw257
756 Rankin EB, Biju MP, Liu Q, Unger TL, Rha J, Johnson RS, Simon MC, Keith B, Haase VH.
757 2007. Hypoxia-inducible factor-2 (HIF-2) regulates hepatic erythropoietin in vivo. *J Clin*
758 *Invest* **117**:1068–1077. doi:10.1172/JCI30117
759 Raval RR, Lau KW, Tran MGB, Sowter HM, Mandriota SJ, Li J-L, Pugh CW, Maxwell PH, Harris
760 AL, Ratcliffe PJ. 2005. Contrasting properties of hypoxia-inducible factor 1 (HIF-1) and
761 HIF-2 in von Hippel-Lindau-associated renal cell carcinoma. *Mol Cell Biol* **25**:5675–5686.
762 doi:10.1128/MCB.25.13.5675-5686.2005
763 Rohs R, Jin X, West SM, Joshi R, Honig B, Mann RS. 2010. Origins of specificity in protein-DNA
764 recognition. *Annu Rev Biochem* **79**:233–269. doi:10.1146/annurev-biochem-060408-
765 091030
766 Sabari BR, Dall'Agnese A, Boija A, Klein IA, Coffey EL, Shrinivas K, Abraham BJ, Hannett NM,
767 Zamudio AV, Manteiga JC, Li CH, Guo YE, Day DS, Schuijers J, Vasile E, Malik S,
768 Hnisz D, Lee TI, Cisse II, Roeder RG, Sharp PA, Chakraborty AK, Young RA. 2018.
769 Coactivator condensation at super-enhancers links phase separation and gene control.
770 *Science* **361**:eaar3958. doi:10.1126/science.aar3958
771 Schödel J, Grampp S, Maher ER, Moch H, Ratcliffe PJ, Russo P, Mole DR. 2016. Hypoxia,
772 Hypoxia-inducible Transcription Factors, and Renal Cancer. *Eur Urol* **69**:646–657.
773 doi:10.1016/j.eururo.2015.08.007
774 Schödel J, Oikonomopoulos S, Ragoussis J, Pugh CW, Ratcliffe PJ, Mole DR. 2011. High-
775 resolution genome-wide mapping of HIF-binding sites by ChIP-seq. *Blood* **117**:e207–
776 e217. doi:10.1182/blood-2010-10-314427

777 Semenza GL. 2012. Hypoxia-Inducible Factors in Physiology and Medicine. *Cell* **148**:399–408.
778 doi:10.1016/j.cell.2012.01.021
779 Shen C, Beroukhim R, Schumacher SE, Zhou J, Chang M, Signoretti S, Kaelin WG. 2011.
780 Genetic and Functional Studies Implicate HIF1α as a 14q Kidney Cancer Suppressor
781 Gene. *Cancer Discov* **1**:222–235. doi:10.1158/2159-8290.CD-11-0098
782 Smythies JA, Sun M, Masson N, Salama R, Simpson PD, Murray E, Neumann V, Cockman ME,
783 Choudhry H, Ratcliffe PJ, Mole DR. 2019. Inherent DNA-binding specificities of the HIF-
784 1α and HIF-2α transcription factors in chromatin. *EMBO Rep* **20**:e46401.
785 doi:10.15252/embr.201846401
786 Srivastava D, Mahony S. 2020. Sequence and chromatin determinants of transcription factor
787 binding and the establishment of cell type-specific binding patterns. *Biochim Biophys*
788 *Acta Gene Regul Mech* **1863**:194443. doi:10.1016/j.bbagrm.2019.194443
789 Swiatek M, Jancewicz I, Kluebsoongnoen J, Zub R, Maassen A, Kubala S, Udomkit A, Siedlecki
790 JA, Sarnowski TJ, Sarnowska E. 2020. Various forms of HIF-1α protein characterize the
791 clear cell renal cell carcinoma cell lines. *IUBMB Life* **72**:1220–1232.
792 doi:10.1002/iub.2281
793 Testa A, Donati G, Yan P, Romani F, Huang TH-M, Viganò MA, Mantovani R. 2005. Chromatin
794 immunoprecipitation (ChIP) on chip experiments uncover a widespread distribution of
795 NF-Y binding CCAAT sites outside of core promoters. *J Biol Chem* **280**:13606–13615.
796 doi:10.1074/jbc.M414039200
797 Tjian R, Maniatis T. 1994. Transcriptional activation: a complex puzzle with few easy pieces.
798 *Cell* **77**:5–8. doi:10.1016/0092-8674(94)90227-5
799 Tokunaga M, Imamoto N, Sakata-Sogawa K. 2008. Highly inclined thin illumination enables
800 clear single-molecule imaging in cells. *Nat Methods* **5**:159–161. doi:10.1038/nmeth1171
801 Varma S, Cohen HJ. 1997. Co-transactivation of the 3' erythropoietin hypoxia inducible
802 enhancer by the HIF-1 protein. *Blood Cells Mol Dis* **23**:169–176.
803 doi:10.1006/bcmd.1997.0134
804 Völkel S, Stielow B, Finkernagel F, Stiewe T, Nist A, Suske G. 2015. Zinc Finger Independent
805 Genome-Wide Binding of Sp2 Potentiates Recruitment of Histone-Fold Protein Nf-y
806 Distinguishing It from Sp1 and Sp3. *PLoS Genet* **11**:e1005102.
807 doi:10.1371/journal.pgen.1005102
808 Wallace EM, Rizzi JP, Han G, Wehn PM, Cao Z, Du X, Cheng T, Czerwinski RM, Dixon DD,
809 Goggin BS, Grina JA, Halfmann MM, Maddie MA, Olive SR, Schlachter ST, Tan H,
810 Wang B, Wang K, Xie S, Xu R, Yang H, Josey JA. 2016. A Small-Molecule Antagonist of

811 HIF2α Is Efficacious in Preclinical Models of Renal Cell Carcinoma. *Cancer Res*
812 **76**:5491–5500. doi:10.1158/0008-5472.CAN-16-0473
813 Warnecke C, Zaborowska Z, Kurreck J, Erdmann VA, Frei U, Wiesener M, Eckardt K-U. 2004.
814 Differentiating the functional role of hypoxia-inducible factor (HIF)-1alpha and HIF-
815 2alpha (EPAS-1) by the use of RNA interference: erythropoietin is a HIF-2alpha target
816 gene in Hep3B and Kelly cells. *FASEB J Off Publ Fed Am Soc Exp Biol* **18**:1462–1464.
817 doi:10.1096/fj.04-1640fje
818 Wei M-T, Chang Y-C, Shimobayashi SF, Shin Y, Strom AR, Brangwynne CP. 2020. Nucleated
819 transcriptional condensates amplify gene expression. *Nat Cell Biol* **22**:1187–1196.
820 doi:10.1038/s41556-020-00578-6
821 Wenger RH, Stiehl DP, Camenisch G. 2005. Integration of oxygen signaling at the consensus
822 HRE. *Sci Signal* **2005**:re12. doi:10.1126/stke.3062005re12
823 Wu D, Potluri N, Lu J, Kim Y, Rastinejad F. 2015. Structural integration in hypoxia-inducible
824 factors. *Nature* **524**:303–308. doi:10.1038/nature14883
825 Xiang L, Chen K, Yan R, Li W, Xu K. 2020. Single-molecule displacement mapping unveils
826 nanoscale heterogeneities in intracellular diffusivity. *Nat Methods* **17**:524–530.
827 doi:10.1038/s41592-020-0793-0
828 Xu R, Wang K, Rizzi JP, Huang H, Grina JA, Schlachter ST, Wang B, Wehn PM, Yang H, Dixon
829 DD, Czerwinski RM, Du X, Ged EL, Han G, Tan H, Wong T, Xie S, Josey JA, Wallace
830 EM. 2019. 3-[(1S,2S,3R)-2,3-Difluoro-1-hydroxy-7-methylsulfonylindan-4-yl]oxy-5-
831 fluorobenzonitrile (PT2977), a Hypoxia-Inducible Factor 2α (HIF-2α) Inhibitor for the
832 Treatment of Clear Cell Renal Cell Carcinoma. *J Med Chem* **62**:6876–6893.
833 doi:10.1021/acs.jmedchem.9b00719
834 Zhang Y, Liu T, Meyer CA, Eeckhoute J, Johnson DS, Bernstein BE, Nusbaum C, Myers RM,
835 Brown M, Li W, Liu XS. 2008. Model-based analysis of ChIP-Seq (MACS). *Genome Biol*
836 **9**:R137. doi:10.1186/gb-2008-9-9-r137
837

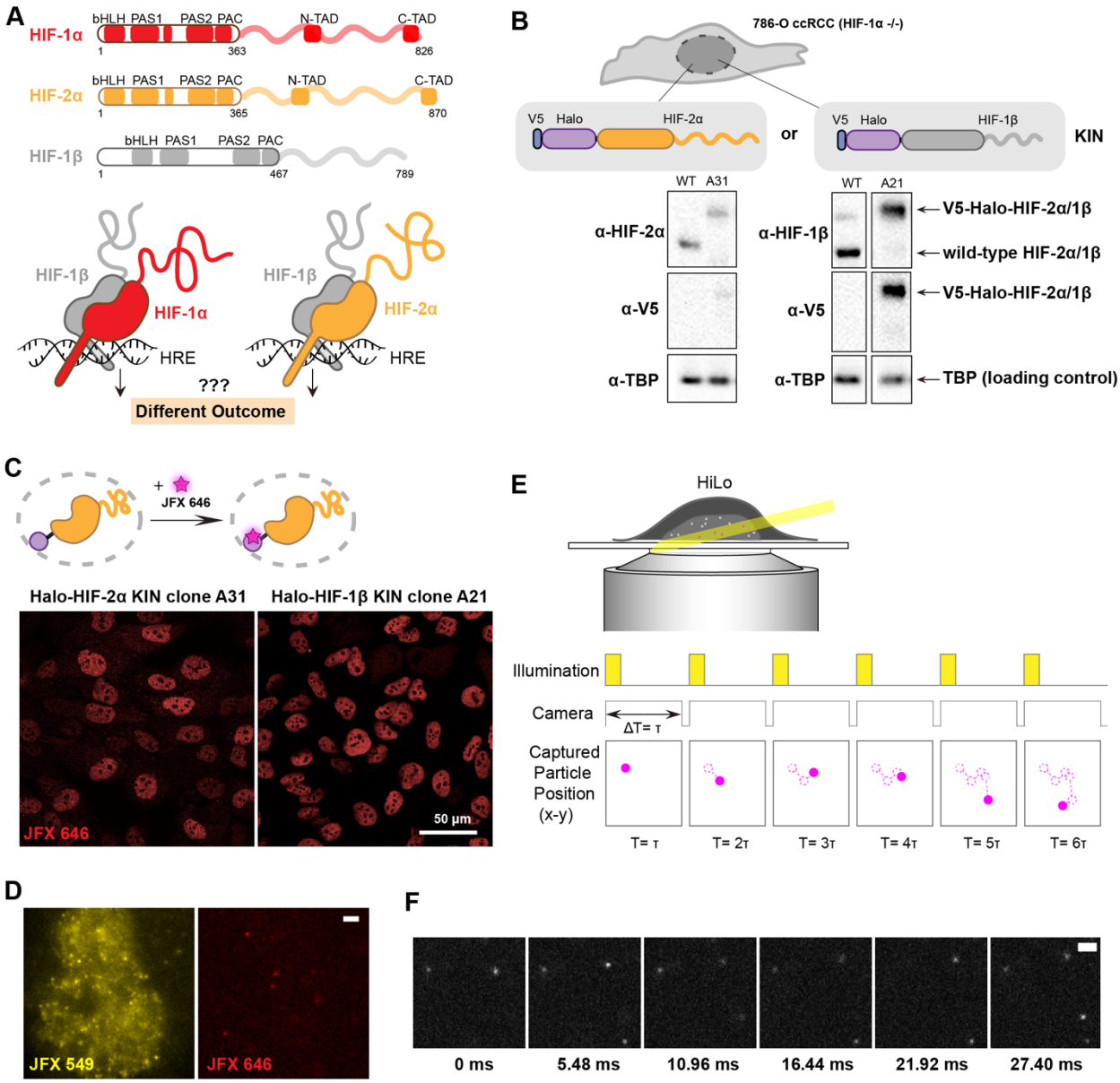

Fig 1. Endogenous tagging of HIFs in 786-O clear cell renal cell carcinoma (ccRCC) cells for fast single particle tracking (fSPT). (A) Schematic showing the similar domain organizations of HIFs (top) and the HRE-bound HIF α/β dimers (bottom). Disordered regions are represented as wavy lines. **(B)** Generation of Halo-KIN clones in the HIF-1α negative 786-O ccRCC line. Top: Halo-tagging scheme of HIF-2α (left) and HIF-1β (right). Bottom: Western blot of wild-type (WT) 786-O cells and homozygously tagged knock-in clones (A31 and A21). See supplemental figure 2 for uncropped images. **(C)** Halo-tagged HIF-2α and HIF-1β show predominant nuclear localization. Top: schematic of labeling Halo-tagged proteins in live cells with cell-permeable Halo-binding JFX646 dye. Bottom: representative images of Halo-HIF-2α (left) and Halo-HIF-1β (right)

847 clones labeled with 500 nM JFX646 **(D)** representative images showing the same cell labeled with
848 a high concentration of JFX549 dye for localizing the nucleus in one channel (left) and labeled
849 sparsely with JFX646 dye for tracking individual molecules in another channel (right). **(E)**
850 Graphical illustration of fSPT capturing trajectories of moving particles. Top: highly inclined and
851 laminated optical sheet illumination (HiLo). Bottom: Illumination and camera sequence with
852 corresponding particle position at each frame (solid magenta dots). Particle's past positions
853 (dashed magenta circles) are connected with dotted magenta lines to show the particle's
854 trajectory. **(F)** Actual data showing detection of Halo-HIF-2α protein molecules at 5.48 ms frame
855 rate.

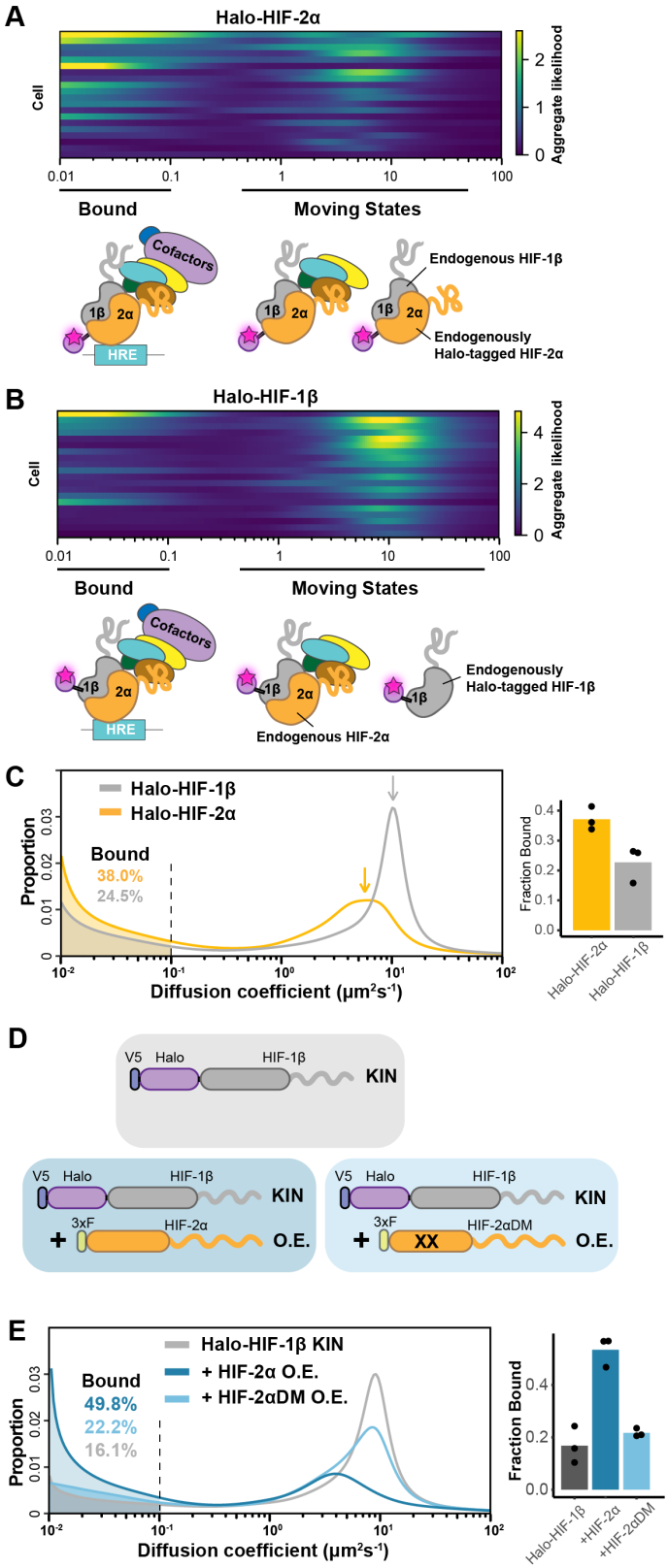

856 **Fig 2. fSPT sensitively detects molecules in a range of states. (A-B)** Likelihood of diffusion

857 coefficients based on a model of regular Brownian motion with localization error (RBME) (Heckert
858 et al., 2021), for (A) Halo-HIF-2α, clone A31 and (B) Halo-HIF-1β, clone A21, with drawing
859 illustrating bound and different hypothetical moving states: complexes, dimer and monomer. Each
860 row represents data collected from one cell. 0.1 μm^2/sec is used as the cut-off for bound versus
861 free. **(C)** Left: proportion of molecules as a function of their diffusion coefficients (posterior mean
862 occupations for a state array (Heckert et al., 2021)) evaluated on trajectories across all cells
863 measured for each KIN line (Halo-HIF-2α, clone A31 and Halo-HIF-1β, clone A21). Compared to
864 HIF-2α, HIF-1β has less bound fraction (grey versus yellow shaded areas) and faster diffusion
865 coefficient (grey versus yellow arrows). Right: Summary of the bound fraction for the two clones.
866 Each bar represents the averaged value from three independent measurements on different days
867 (black dots). **(D-E)** Over-expressing HIF-2α, but not a dimerization mutant form, in the Halo-HIF-
868 1β knock-in (KIN) line increases HIF-1β binding and decreases its diffusion coefficient. (D)
869 schematic illustrating the parental Halo-HIF-1β KIN cells (grey background) and cells stably over-
870 expressing (O.E.) either the wild type (darker blue background) or a dimerization mutant (DM,
871 black crosses, lighter blue background) form of HIF-2α. (E) Left: Proportion of molecules as a
872 function of diffusion coefficient measured for HIF-1β in Halo-HIF-1β KIN cells (grey) and in Halo-
873 HIF-1β KIN cells overexpressing HIF-2α (WT, dark blue background, or dimerization mutant (HIF-
874 2αDM), light blue). Shaded areas indicate bound fraction. Right: Bar plot of the average value
875 (bar height) of the bound fraction calculated from three independent measurements (black dots)
876 for each condition.

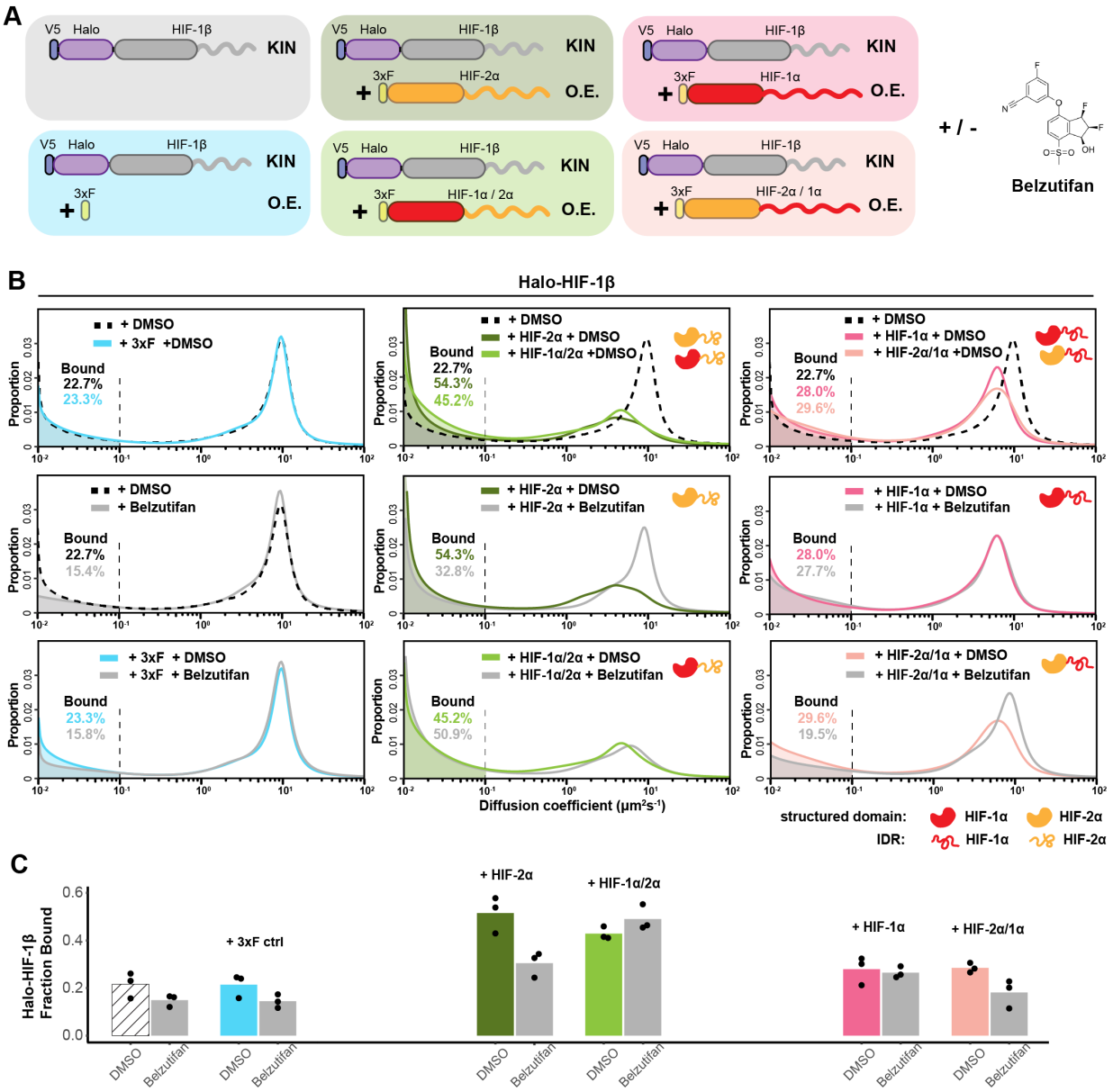

Fig 3. HIF-α increases HIF-1β binding and decreases HIF-1β diffusion coefficient through dimerization, in an IDR-dependent manner. (A) Schematic of evaluating Halo-HIF-1β behavior with genetic and small-molecule perturbation. Parental Halo-HIF-1β knock-in (KIN) cells (grey background) and cells stably overexpressing (O.E.) either a certain form of HIF-α (WT or domain swap, HIF-1α, red, HIF-2α, orange. Disordered regions are represented as wavy lines.) (various colored background) or a 3xFLAG tag only control (blue background) are used, with and without 0.2 μM Belzutifan (HIF-2α/1β dimerization inhibitor) treatment. **(B)** Proportion of Halo-HIF-1β molecules as a function of diffusion coefficient measured in various conditions outlined in (A) Top row: DMSO only, showing overexpressing α subunit can change HIF-1β behavior. Cells over-

886 expressing the α subunit variants containing HIF-2α disordered region (orange curly line) have a
887 stronger effect (middle, HIF-2α and HIF-1α/2α,) compared to those containing HIF-1α disordered
888 region (right, HIF-1α and HIF-2α/1α). Middle and Bottom rows: proportions of HIF-1β as a function
889 of diffusion coefficient, measured in each of the 6 cell lines with Belzutifan treatment are compared
890 to the DMSO control. Changes caused by overexpressing an α subunit can be specifically
891 reverted by Belzutifan treatment for cell lines expressing an α subunit variant that contains the
892 HIF-2α structured domain (orange globule). **(C)** Summary of the average bound fractions for all
893 12 conditions, with black dots indicating values from each of the three individual measurements.

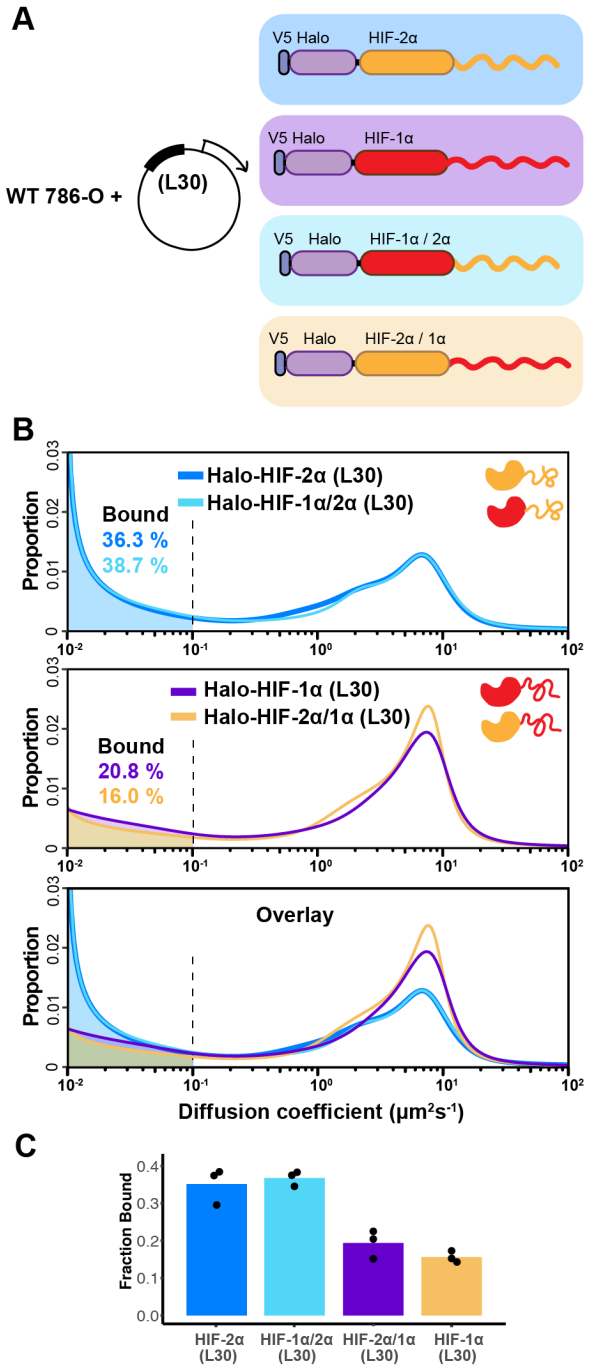

Fig 4. The IDR governs HIF-α molecular dynamics and binding characteristics. (A) Schematic representation of different HIF (WT and domain-swapped) being weakly and stably overexpressed with an L30 promoter and tracked in WT 786-O cells. **(B)** Proportion of molecules as a function of diffusion coefficient for every tracked protein in (A). Top: overlapping distribution curves shows almost identical behavior between Halo-HIF-2α (dark blue curve) and Halo-HIF-1α/2α (light blue curve). Middle: similar behavior between Halo-HIF-1α (purple curve) and Halo-

900 HIF-2α/1α (yellow curve), bottom: overlay of all four curves shows very different behavior between
901 proteins containing 1α versus 2α IDR. **(C)** Bar plot comparing the average bound fraction for cells
902 in (B), with black dots indicating values from three independent measurements.

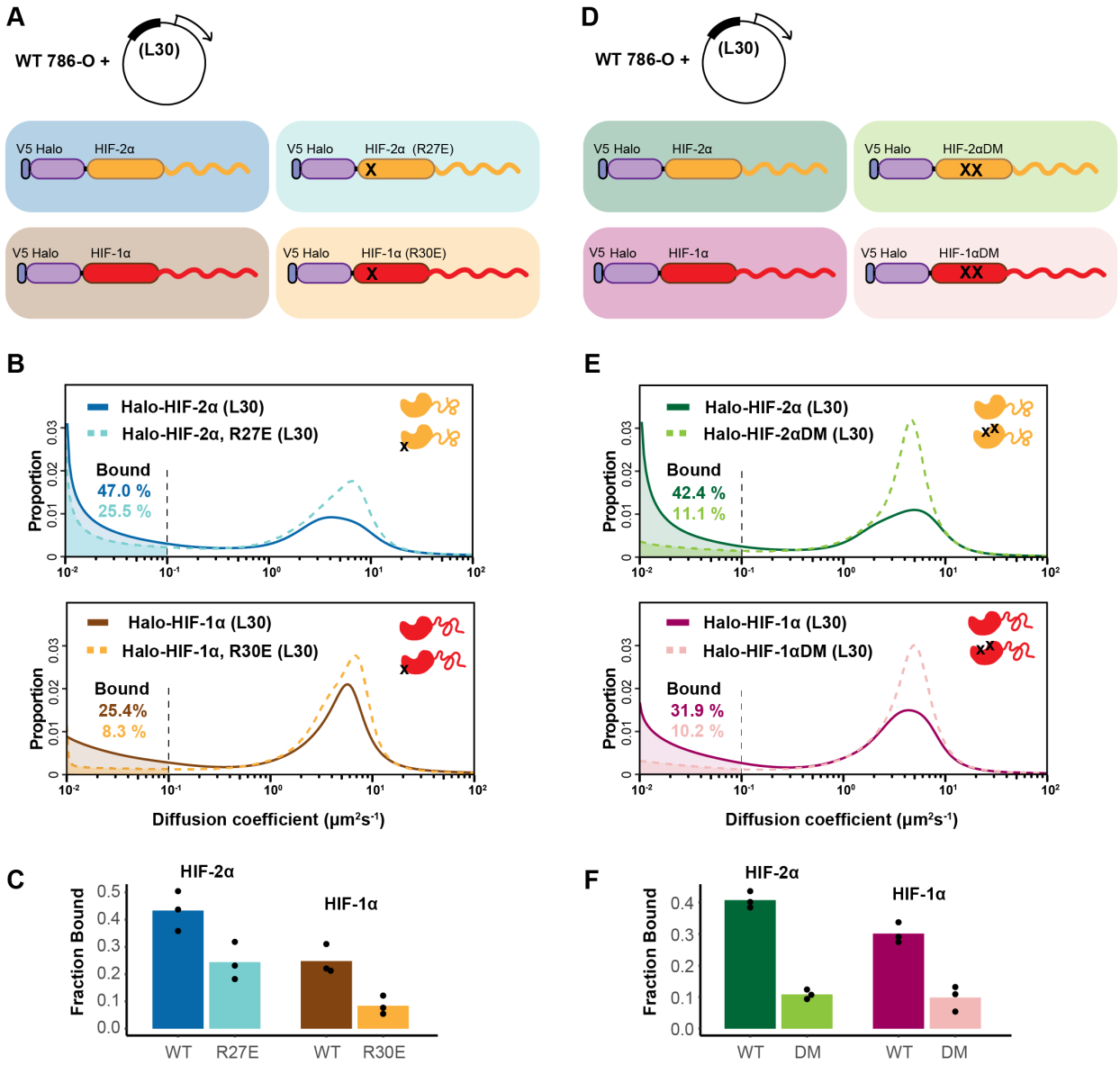

Fig 5. HIF-α IDR alone is not sufficient for binding. (A-C) Mutation in DBD reduces the bound fraction for both HIF-α isoforms. (A) Schematic representation of weakly overexpressing and tracking wild type and DBD mutant (R27E or R30E, black cross) forms of HIF-1α or 2α, using the same L30 expression system as in Fig 5. (B) Proportion of molecules as a function of diffusion coefficient for tracked protein listed in (A). (C) Bar plot summarizes the average bound fraction (height of the bar) of three independent measurements (black dots). **(D-F)** Mutations in the dimerization domain reduce the bound fraction for both HIF-α isoforms but do not change their diffusion coefficient. (D) Schematic representation of weakly over-expressing and tracking wild type and dimerization-mutant (DM, two black crosses) forms of Halo-HIF-1α or -2α, using the L30 expression system. (E) Proportion of molecules as a function of diffusion coefficient for tracked

913 protein in (D). (F) Summary of the average bound fraction for all four proteins with black dots
914 indicating values from three independent measurements.

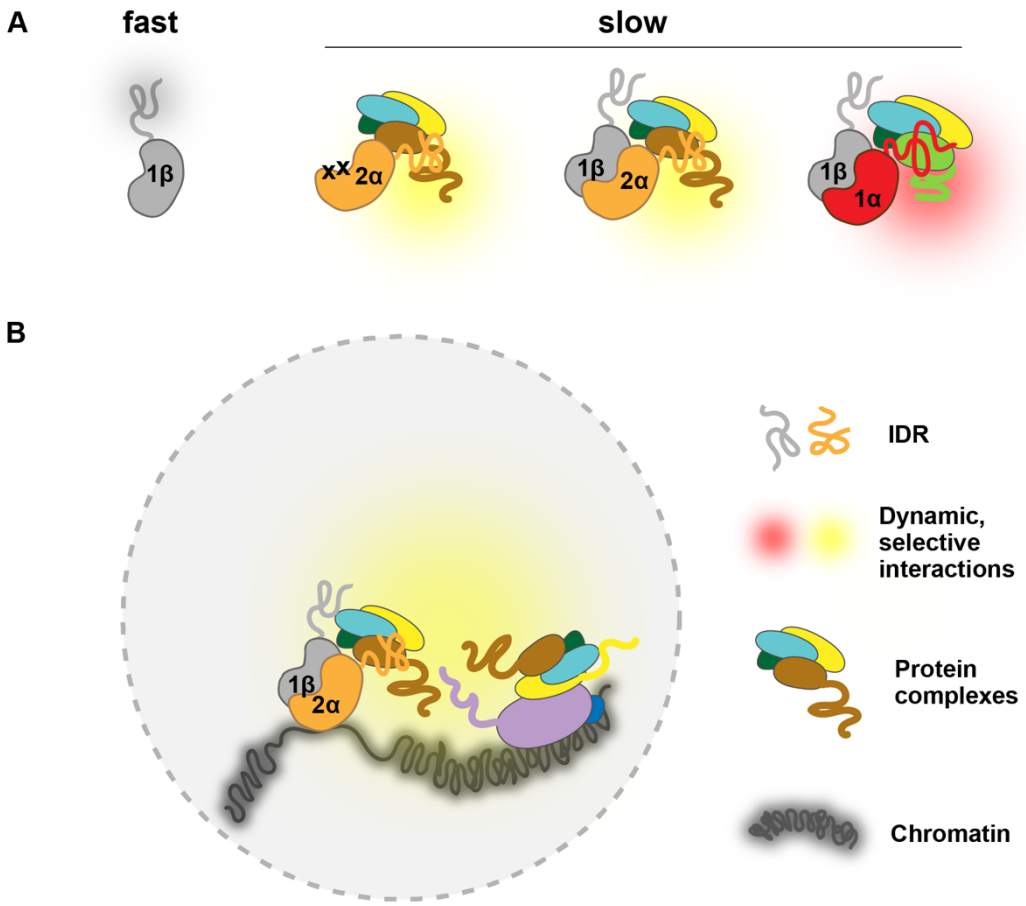

Fig 6. A model for IDR-mediated nuclear search and chromatin binding. (A) The HIF-α IDR determines its slow motion of both the HIF-α monomer and HIF-α/β dimer, likely by HIF-α IDR mediated interactions with nuclear macromolecules. For HIF-α, the IDR thus determines its slow motion regardless of its dimerization status. For HIF-1β, dimerization slows it down due to extra interactions (yellow and red clouds) brought by HIF-α IDR. **(B)** As an obligated dimer, the DBD and the dimerization domain are both necessary for HIF binding, but the IDR determines the degree of binding, possibly via its interaction with nearby macromolecules, including other proteins and/or nucleic acids (DNA and/or RNA).

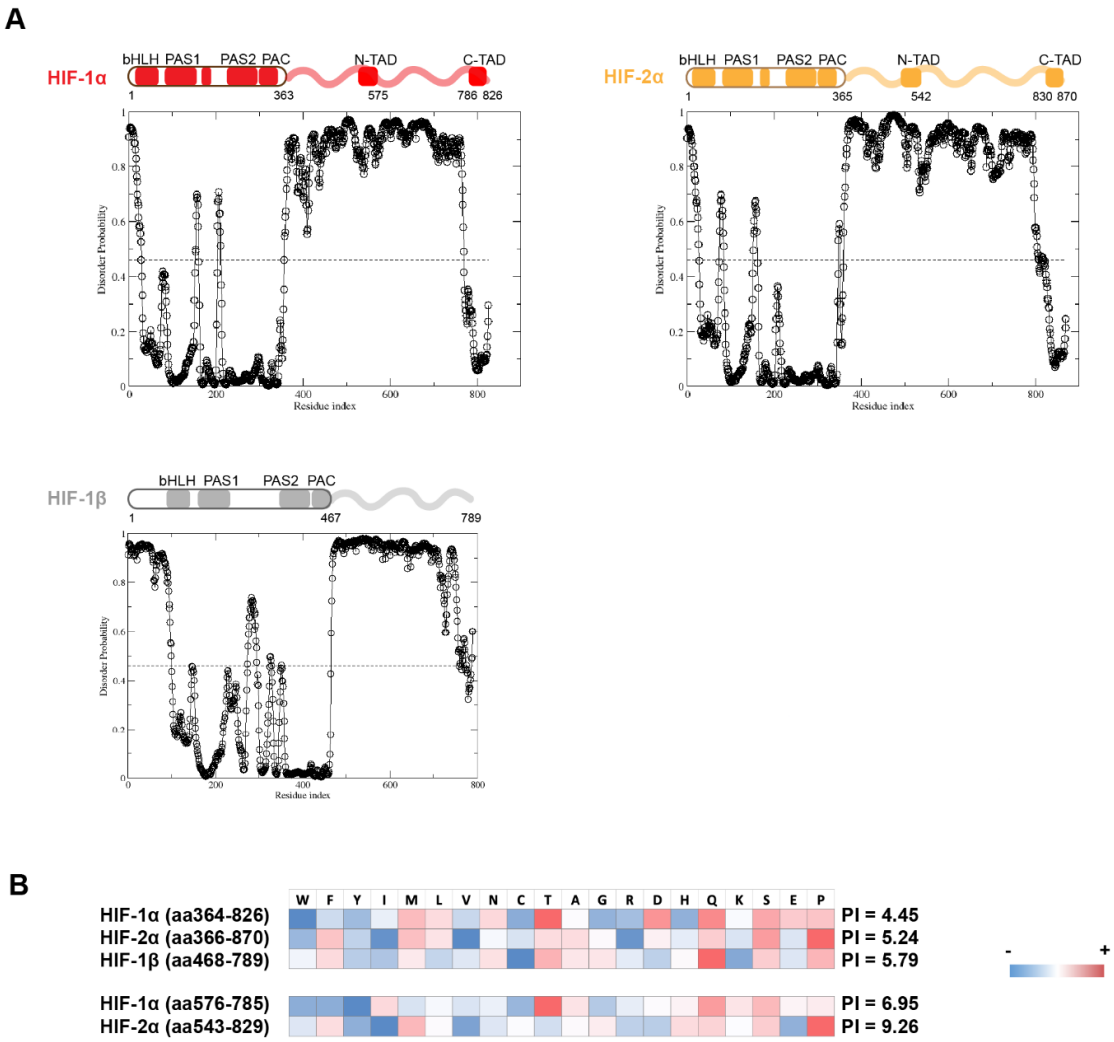

Fig S1. Domain analysis of HIFs. (A) Disorder propensity of HIF-1α, -2α and -1β, predicted by SPOT-Disorder (Hanson et al., 2017). High values indicate higher disorder propensity. **(B)** HIF-1α and HIF-2α IDRs have different amino acid composition biases. The relative enrichment for each amino acid is calculated by comparison with the average amino acid composition of non-membrane proteins in vertebrates (Gaur, 2014), and color coded, with red indicating relative high enrichment and blue indicating relative depletion. The IDR segments between the N-TAD and C-TAD are especially different between HIF-1α and HIF-2α in terms of acidity (bottom).

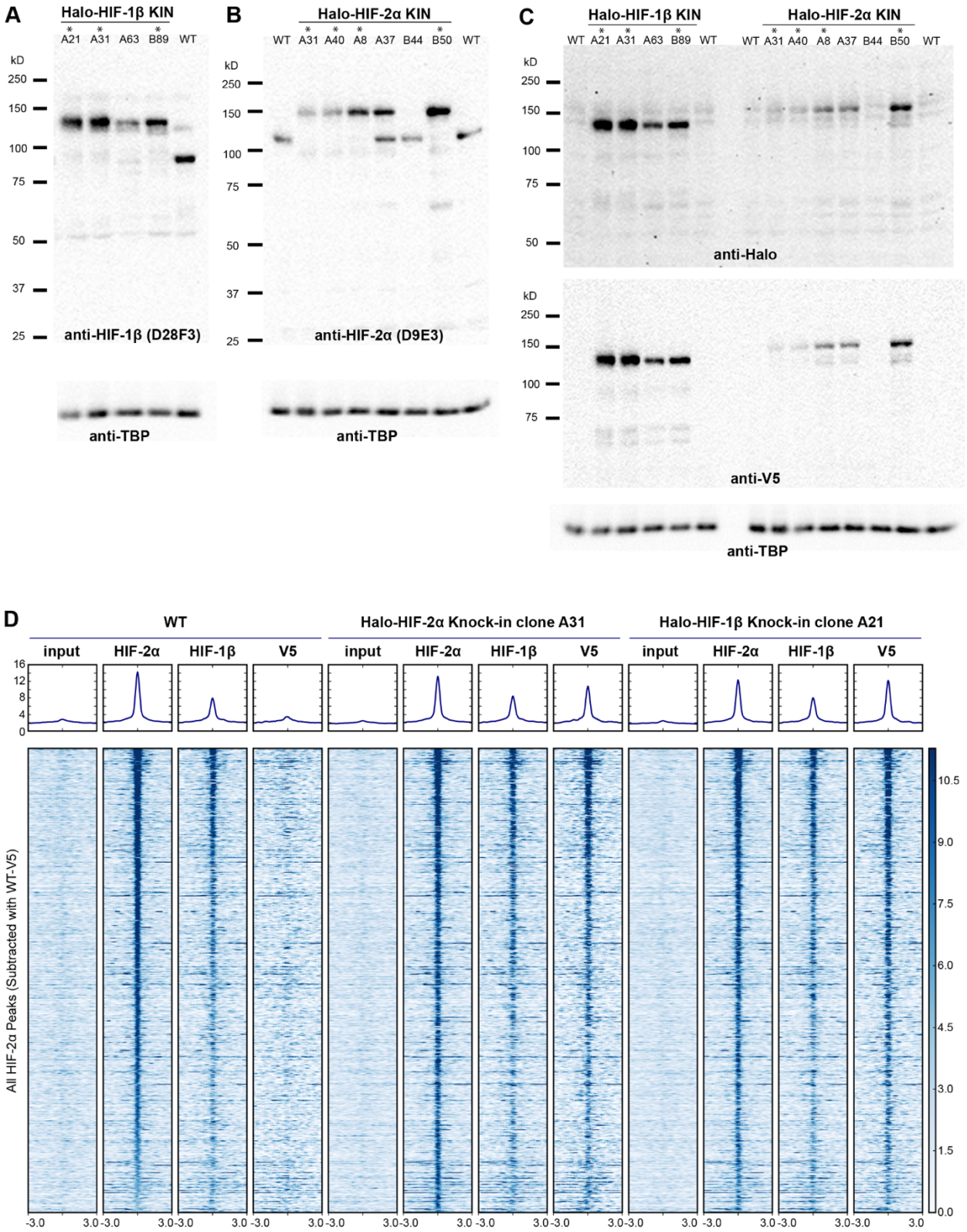

930 **Fig S2. Verification of endogenous tagging of HIFs in 786-O ccRCC cells. (A) (B) (C)**
931 Uncropped images of western blot of wild-type (WT) 786-O cells and homozygously tagged

932 knock-in clones (*). (A) HIF-2α protein is detected in WT and various KIN clones with a Rabbit
933 monoclonal antibody against HIF-2α (Cell Signaling, D9E3), membranes were stripped and
934 reblotted for TBP for loading control. (B) HIF-1β protein is detected in WT and various KIN clones
935 with a Rabbit monoclonal antibody against HIF-1β (Cell Signaling, D28F3), membranes were
936 stripped and reblotted for TBP for loading control. (C) Various HIF-2α and HIF-1β KIN clones are
937 loaded on the same gel and probed for tagged protein levels using an anti-Halo antibody (top);
938 the membrane was stripped and reblotted for TBP for loading control, then stripped again and
939 reblotted for V5 tag. Halo-HIF-1β is generally expressed at a much higher level than Halo-HIF-2α,
940 as shown by the detected Halo or V5 level. **(D)** HeatMap of the ChIP-seq experiments comparing
941 binding profiles of HIF-2α and HIF-1β in WT or KIN clones. ChIP-Seq read counts (Reads Per
942 Genomic Content) are plotted at MAC2-called HIF-2α peak regions (across all cell lines and
943 subtracted of V5 peaks called in WT 786-O cells) centered around the peak.

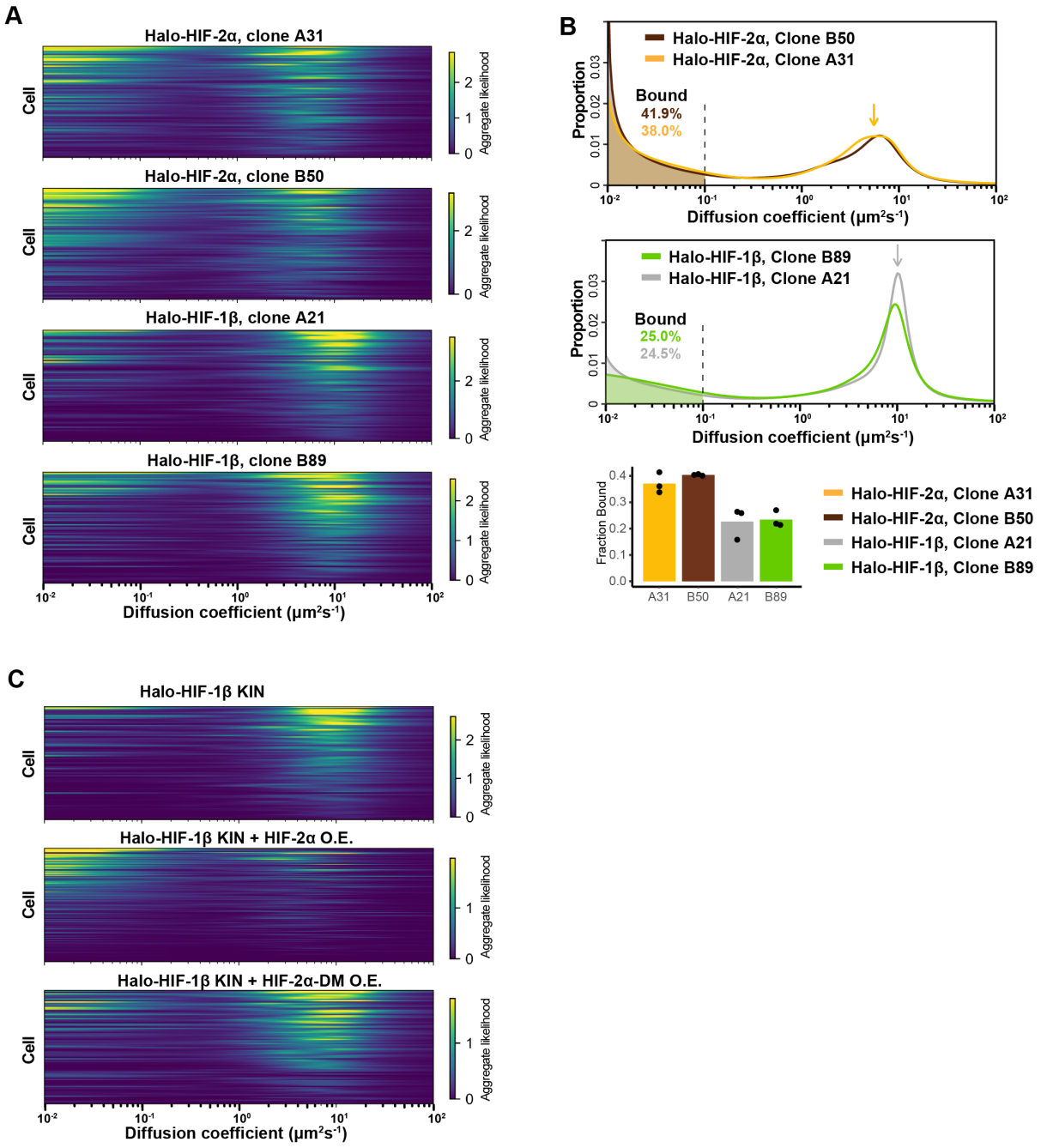

Fig S3. HIF-1β behavior is distinct from HIF-2α and changes as 1β-to-2α stoichiometry changes. (A) RBME likelihood of diffusion coefficient in individual cells for four Halo-HIF-2α or Halo-HIF-1β KIN clonal lines. **(B)** Top and middle: proportion of molecules as a function of their diffusion coefficients (posterior mean occupations for a state array) evaluated on trajectories across all cells measured for additional Halo-HIF KIN line showing reproducible results in different KIN clones (Top, clone A31 and B50 for Halo-HIF-2α KIN and middle, clone A21 and B89 for Halo-HIF-1β KIN). Data for clone A21 and A31 are replotted from Figure 2. Bottom: Summary of

951 the bound fraction for all four cell lines. Each bar represents the average of three independent
952 measurements on different days (black dots). **(C)** RBME likelihood of diffusion coefficient obtained
953 for individual cells in either Halo-HIF-1β KIN cells (top) or Halo-HIF-1β KIN cells overexpressing
954 HIF-2α (WT, middle or DM, bottom).
955

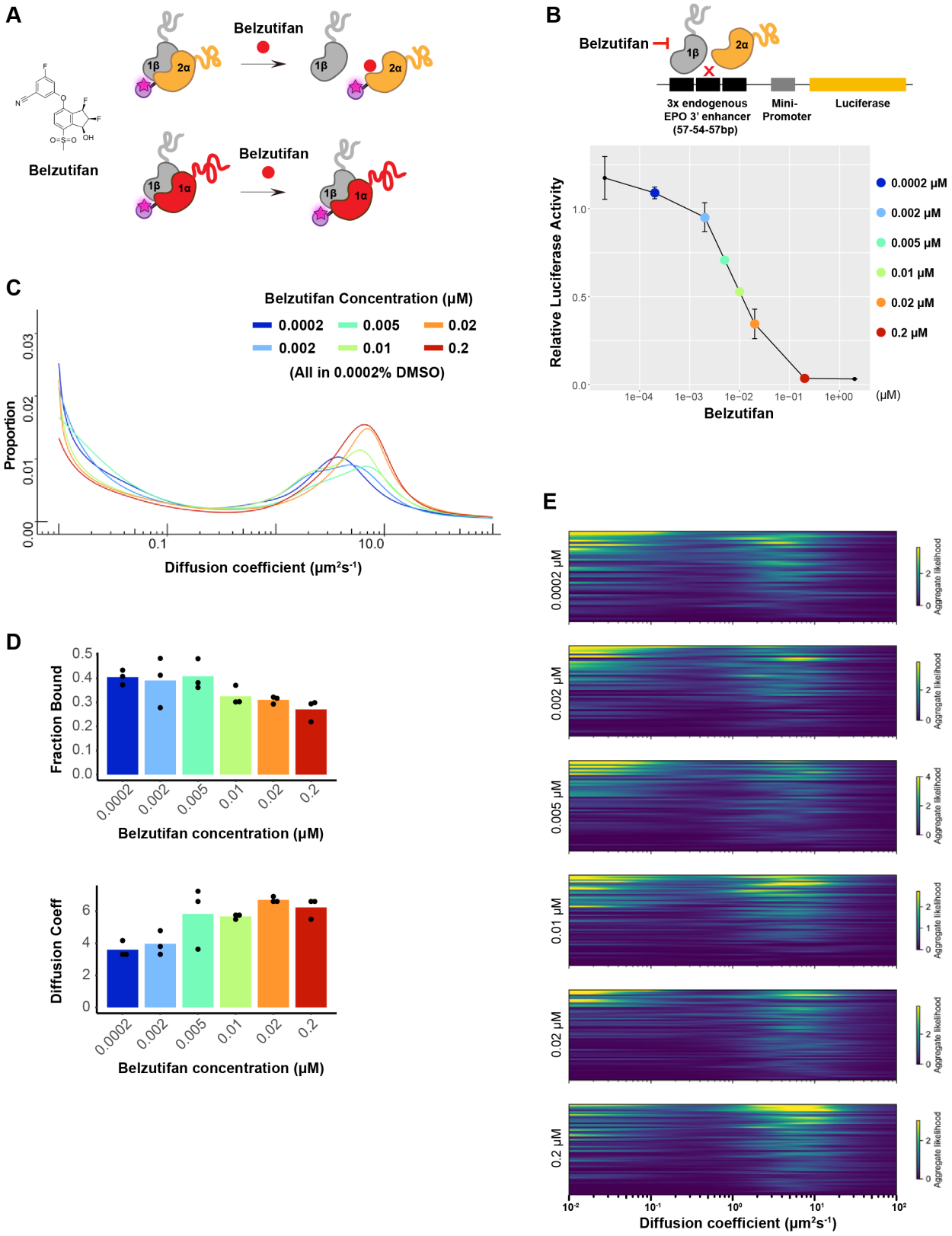

956 **Figure S4. Dosage-dependent inhibition of HIF-2α binding and activity by Belzutifan. (A)**

957 Molecular structure of Belzutifan (PT-2977) and schematic illustration of its function to specifically
958 block dimerization between HIF-2α/1β but not HIF-1α/1β. **(B)** Luciferase assay using an HRE-
959 containing reporter confirms Belzutifan dosage-dependent inhibition of HIF-2α activity. Error bars
960 represent SE. **(C)** Proportion of molecules as a function of diffusion coefficient for HIF-2α
961 measured in Halo-HIF-2α KIN line clone A31 treated with different concentrations of Belzutifan.
962 DMSO levels are kept the same for all conditions at 0.0002%. **(D)** The average fraction bound
963 decreases (top) and the average peak position diffusion coefficient increases (bottom) at
964 increasing doses of Belzutifan. Individual measurements are indicated as black dots. **(E)** RBME
965 likelihood of diffusion coefficient in individual cells for all six drug dosages.

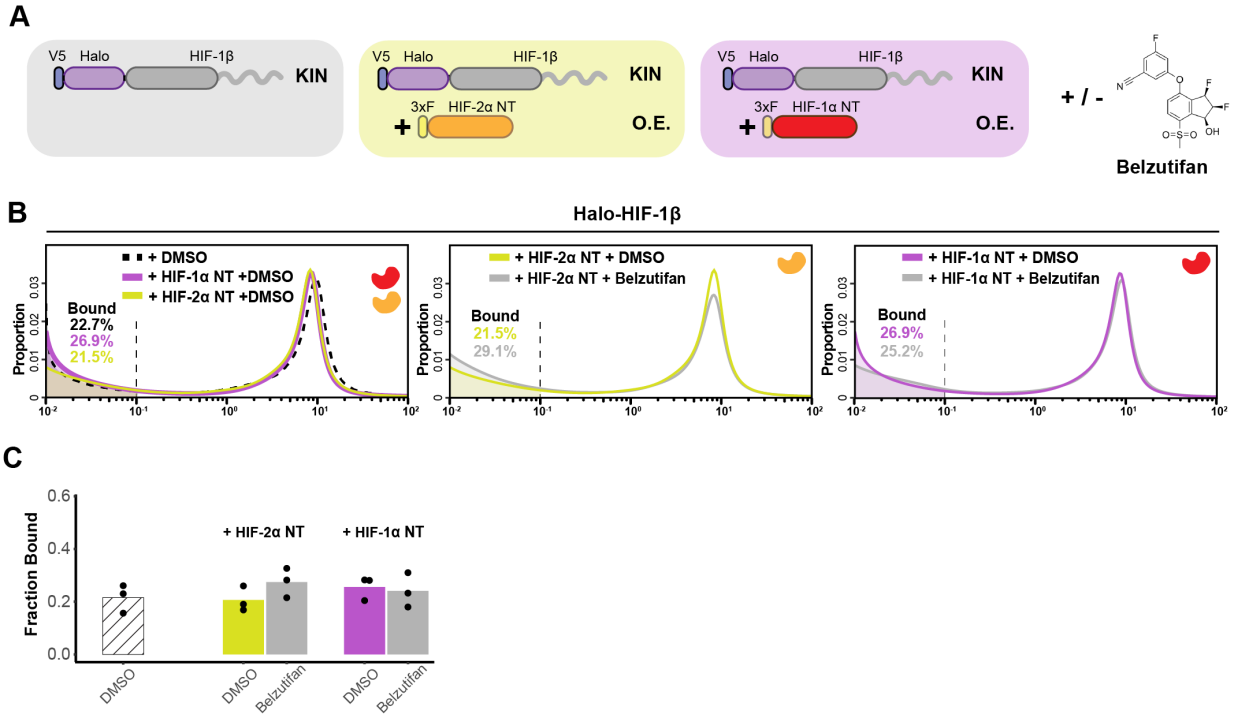

Figure S5. Additional data for figure 3 showing HIF-α without the IDR is not able to increase HIF-1β binding or decrease its diffusion coefficient (A) Schematic of evaluating Halo-HIF-1β behavior while overexpressing only the N-terminal structured region (NT) of HIF-α in combination with small molecule perturbation. Parental Halo-HIF-1β KIN cells (grey background, same as in figure 3) and cells stably overexpressing (O.E.) either HIF-2α NT (orange in yellow background) or HIF-1α NT (red in purple background) are used, with and without treatment with 0.2-μM Belzutifan. **(B)** Proportion of HIF-1β molecules as a function of diffusion coefficient measured in various cells outlined in (A). Left: treated with DMSO only, comparing HIF-1β behavior in the parental cells (black dashed curve, same as in figure 3) and in cells expressing either HIF-1α NT (purple curve) or HIF-2α NT (yellow curve). Middle and right: proportions of HIF-1β as a function of diffusion coefficient, measured in cells expressing either HIF-1α NT (right) or HIF-2α NT (middle) with Belzutifan treatment (grey curves), compared to the DMSO control (purple or yellow curves). **(C)** Summary of the average bound fractions for conditions in (B), with black dots indicating values from each of the three individual measurements.

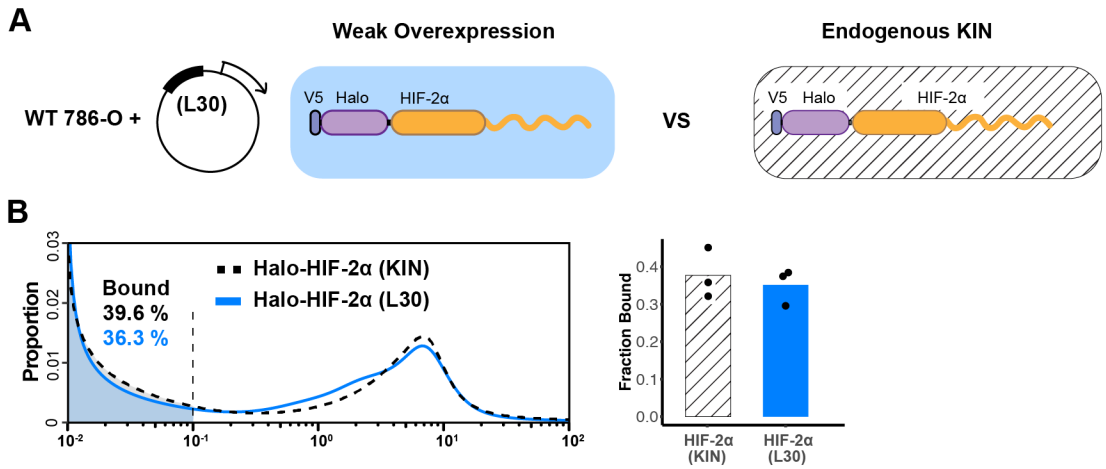

Figure S6. L30 weak expression system is able to recapitulate the endogenous protein behavior. (A) Schematic of the L30 overexpression system where Halo-HIF-2α is weakly expressed with an L30 promoter in wild-type 786-O cells (left) and Knock-in cells where HIF-2α is endogenously tagged and expressed (right). **(B)** Comparison between endogenous Halo-HIF-2α (KIN) and Halo-HIF-2α over-expressed with L30 promoter (L30), showing very similar behavior. Left: Proportion of Halo-HIF-2α as a function of diffusion coefficient and the corresponding bound fraction (shaded area). Right: Bar plot summarize the average bound fraction with three independent measurements (black dots).

989 **Supplementary Table 1. Constructs for stable cell lines**
990

Name	promoter	Gene product	Short name in the paper	Appeared in
PB EF1a 3XF EX-MCS IRES Puro	EF1a	3xFLAG tag	3xF	Fig. 3
PB EF1a 3XF-GDGAGLIN-hEPAS1 IRES Puro	EF1a	HIF-2α N-terminally fused with 3xFLAG tag through a short peptide linker sequence (GDGAGLIN)	HIF-2α	Fig. 2 Fig. 3 Fig. S3
PB EF1a 3XF-GDGAGLIN-hEPAS1_R171A-V192D IRES Puro	EF1a	HIF-2α dimerization mutant (R171A-V192D) N-terminally fused with 3xFLAG tag through a short peptide linker sequence (GDGAGLIN)	HIF-2α DM	Fig. 2 Fig. S3
PB EF1a 3XF-EPAS1_365 IRES Puro	EF1a	The N terminal region of HIF-2α (aa 1-365) N-terminally fused with 3xFLAG tag	HIF-2α NT	Fig. S5
PB EF1a 3XF-EPAS1_365-364_HIF1a IRES Puro	EF1a	HIF-2α/1α chimera protein (aa 1-365 of HIF-2α and aa 364-826 of HIF-1α) N-terminally fused with 3xFLAG tag	HIF-2α/1α	Fig. 3
PB EF1a 3XF-GDGAGLIN-hHIF1a IRES Puro	EF1a	HIF-1α N-terminally fused with 3xFLAG tag through a short peptide linker sequence (GDGAGLIN)	HIF-1α	Fig. 3
PB EF1a 3XF-HIF1a_363 IRES Puro	EF1a	The N terminal region of HIF-1α (aa 1-363) N-terminally fused with 3xFLAG tag	HIF-1α NT	Fig. S5
PB EF1a 3XF-HIF1a_363-366_EPAS1 IRES Puro	EF1a	HIF-1α/2α chimera protein (aa 1-363 of HIF-1α and aa 366-870 of HIF-2α) N-terminally fused with 3xFLAG tag	HIF-1α/2α	Fig. 3
PB L30prom V5-Halo-GDGAGLIN-hEPAS1 IRES Puro	L30	HIF-2α N-terminally fused with V5-HaloTag through a short peptide linker sequence (GDGAGLIN)	Halo-HIF-2α (L30)	Fig. 4 Fig. S6
PB L30prom V5-Halo-GDGAGLIN-hEPAS1_365-364_HIF1a IRES Puro	L30	HIF-2α/1α chimera protein (aa 1-365 of HIF-2α and aa 364-826 of HIF-1α) N-terminally fused with V5-HaloTag through a short peptide linker sequence (GDGAGLIN).	Halo-HIF-2α/1α (L30)	Fig. 4
PB L30prom V5-Halo-GDGAGLIN-hHIF1a IRES Puro	L30	HIF-1α N-terminally fused with V5-HaloTag through a short peptide linker sequence (GDGAGLIN)	Halo-HIF-1α (L30)	Fig. 4
I_PB L30prom V5-Halo-GDGAGLIN-	L30	HIF-1α/2α chimera protein (aa 1-363 of HIF-1α and aa 366-	Halo-HIF-1α/2α (L30)	Fig. 4

HIF1A_363-366_EPAS1 IRES Puro		870 of HIF-2α) N-terminally fused with V5-HaloTag through a short peptide linker sequence (GDGAGLIN).		
PB L30prom V5-Halo-GDGAGLIN-hEPAS1 IRES Puro_R27E	L30	HIF-2α DBD mutant (R27E) N-terminally fused with V5-HaloTag through a short peptide linker sequence (GDGAGLIN).	Halo-HIF-2α, R27E (L30)	Fig. 5
PB L30prom V5-Halo-GDGAGLIN-hHIF1a IRES Puro_R30E	L30	HIF-1α DBD mutant (R30E) N-terminally fused with V5-HaloTag through a short peptide linker sequence (GDGAGLIN).	Halo-HIF-1α, R30E (L30)	Fig. 5
PB L30prom V5-Halo-GDGAGLIN-hEPAS1_R171A-V192D IRES Puro	L30	HIF-2α dimerization mutant (R171A-V192D) N-terminally fused with V5-HaloTag through a short peptide linker sequence (GDGAGLIN).	Halo-HIF-2α DM (L30)	Fig. 5
PB L30prom V5-Halo-GDGAGLIN-hHIF1a_R170A-V191D IRES Puro	L30	HIF-1α dimerization mutant (R170A-V191D) N-terminally fused with V5-HaloTag through a short peptide linker sequence (GDGAGLIN).	Halo-HIF-1α DM (L30)	Fig. 5

991